THESIS FOR THE DEGREE OF LICENTIATE OF ENGINEERING

Polymer Brushes for Bioanalytical Applications

The Pore-suit of Functional Nanostructures

Jesper Medin

Department of Chemistry & Chemical Engineering
CHALMERS UNIVERSITY OF TECHNOLOGY
Göteborg, Sweden 2025

Polymer Brushes for Bioanalytical Applications

The Pore-suit of Functional Nanostructures

Jesper Medin

Licentiatuppsatser vid Institutionen för kemi och kemiteknik

Chalmers tekniska högskola

Nr 2025:01

Department of Chemistry & Chemical Engineering

Chalmers University of Technology

SE-412 96 Göteborg

Telephone +46 31 772 1000

Cover:
Bioanalytical applications of PNIPAM, PAA and PHEAA brushes. Macromolecular gating is achieved with thermo-responsive PNIPAM, which collapses upon increasing the temperature. Enzymatic biosensing is achieved with PAA brushes, which can be modified to bind enzymes that can generate H_2O_2 that are reactive towards an electrode. Selective transport is achieved with PHEAA, that selectively interacts with polyacids (triangles) while repelling other macromolecules (stars).

Printed by Chalmers digitaltryck

Göteborg, Sweden 2025

Polymer Brushes for Bioanalytical Applications
The Pore-suit of Functional Nanostructures
Jesper Medin
Department of Chemistry & Chemical Engineering
Chalmers University of Technology

Abstract

When polymers are grafted from a surface at a high surface coverage, and exposed to a liquid environment, it promotes stretching of the chains up and perpendicular to the surface, forming a "brush" structure. These nanoscale “polymer brushes” are commonly used as surface coatings for their protein repelling (antifouling) properties, where the polymer brushes prevent proteins and larger molecules from attaching to the surface. However, polymer brushes can also add functionality to the surface by using stimuli-responsive monomers in the polymerisation.

In this work, three bioanalytical applications of functional polymer brushes have been investigated. Thermo-responsive poly(*N*-isopropylacrylamide) (PNIPAM) was used for long-term stable trapping of enzymes in nanoscale chambers (one attoliter large). Once trapped in the chambers, the enzymes were demonstrated to retain their activity and were successfully used in enzymatic reactions, including the conversion of lactose to d-glucono-1,5-lactone and cycling of the cofactor nicotinamide (NADH) and its oxidised equivalent (NAD^+). pH-responsive poly(acrylic acid) (PAA) was used for covalent immobilisation of enzymes for biosensing purposes. The immobilised enzymes were demonstrated to react with non-electrochemically active analytes and generate an active product, allowing electrochemical detection of the analyte. This, coupled with the antifouling properties of the brush, allowed for detection of the non-electrochemically active neurotransmitters glutamate and acetylcholine, even in diluted cerebrospinal fluid (CSF), a complex biofluid. Finally, poly(*N*-hydroxyethylacrylamide) (PHEAA) was investigated as a selective diffusion barrier for macromolecular transport of poly(methacrylic acid) shuttles, mimicking the selective transport of the nuclear pore complex (NPC).

Keywords: Poly(*N*-isopropylacrylamide); poly(*N*-hydroxyethylacrylamide); poly(acrylic acid); polymer brushes; biomolecular transport; neurotransmitters; electrochemical sensors; enzymes; nanopore transport; nuclear pore complex mimics

List of Publications

This thesis is based on the following appended papers, referred to by Roman numerals in the text:

I. Stable Trapping of Multiple Proteins at Physiological Conditions using Nanoscale Chambers with Macromolecular Gates

J. Svirelis, Z. Adali†, G. Emilsson†, J. Medin†, J. Andersson, R. Vattikunta, M. Hulander, J. Järlebark, K. Kolman, O. Olsson, Y. Sakiyama, R. Y. H. Lim, A. Dahlin

Nature Communications, 14 **(2023)**, 5131

II. Enzymatic Polymer Brush Interfaces for Electrochemical Sensing in Biofluids

J. Medin, M. Kyriakidou, B. Santoso, P. Gupta, G. Ferrand-Drake del Castillo, A.-S. Cans and A. Dahlin

Submitted. Preprint available. http://dx.doi.org/10.13140/RG.2.2.22114.13769

† These authors contributed equally

My Contributions to the Publications

Paper I

Shared second author. I was responsible for measurements with enzyme cascade reactions, specifically lactose breakdown with a GAL/GOx system and NADH co-factor cycling with an ADH/GOx system. I also performed synthesis of PNIPAM brushes, SPR, QCM-D, and extinction spectroscopy for these experiments.

Paper II

First author. I was responsible for all experimental work except for the development of the PAA brush synthesis protocol, which was done by M. Kyriakidou. I processed all data, wrote the first draft of the manuscript and co-authored the final version.

Additional publications which are not included in the thesis:

Pore performance: artificial nanoscale constructs that mimic the biomolecular transport of the nuclear pore complex

J. Andersson†, J. Svirelis†, J. Medin, J. Järlebark, R. Hailes, A. Dahlin

Nanoscale Advances, 4 **(2022)**, 4925

† These authors contributed equally

Acknowledgements

I would like to thank the Area of Advance Nano and everyone from the Excellence Initiative for funding my PhD and giving me this chance to explore the vast world that is nanomaterials science. The work was mainly performed at the facilities of the Division of Applied Chemistry in the Department of Chemistry and Chemical Engineering at Chalmers University of Technology.

I want to express my sincerest gratitude to my supervisor Prof. Andreas Dahlin for the opportunity to conduct research in his group, for his scientific guidance, and for the interesting discussions we have had over the years. I also want to thank my co-supervisor Prof. Fredrik Westerlund, my examiner Prof. Martin Andersson, and my director of studies Prof. Lars Öhrström, as well as Prof. Ann-Sofie Cans who I have worked with for parts of my studies. Thank you all for your time and your dedication, and for your continued support as I continue my journey.

Thanks to all current and former group members of the functional nanostructures group, Amina, Bagus, Gustav, John, Julia, Justas, Maria, Marika, Oliver, Radhika and Sevil. A special thanks to Bagus for introducing me to the world of polymer brushes; I hope you have a good time down in the warmer climates of Mölndal. I would also like to thank my former students Leyla, Sevda and Xiaohan for all the hard work you have done, I wish you the best for the future.

And last but not least, to my colleagues at the division and to my former, and current, office mates Guido, Eduardo and Nasim, thank you for all the laughs through the years and for creating a great working environment! A special thank you to my Maroula and my family for all your love, care and support. And thank you to you who made it this far, I hope you will enjoy the rest of this thesis!

Jesper Medin, Göteborg, February 2025

Contents

Preface 1

Surface-confined macromolecules known as polymer brushes have found an increasing number of applications in the interdisciplinary fields of nano- and biotechnology over the last decades. This is for their ability to passivate and functionalise substrates with different chemical properties, especially when that substrate in one way or another requires exposure to biological macromolecules; such as proteins. When these biomolecules are allowed to interact with a substrate they have a tendency to adsorb through non-specific[1] interactions, potentially fouling the substrate and limiting its intended function[1]. Furthermore, adsorption can lead to denaturation of the biomolecule, often with irreversible impact on the proteins function and activity[2]. However, by densely tethering polymers to the substrate it is possible to form a "soft" brush-like coating that can prevent this unwanted adsorption, or to allow the biomolecules to adsorb, but in a way where their structures are retained.

1: Non-specific interactions refer to interactions that can occur as a result of the general physiochemical properties of the surface. These include electrostatic forces, dispersive forces, hydrophobic forces, steric forces and hydrogen bonding, amongst others.

The work summarised in this thesis is aimed towards developing polymer brushes for bioanalytical applications involving proteins and complex biofluids[2]. It is based on two manuscripts and some unpublished results from my PhD studies, including how thermo-responsive polymer brushes can be used for biomolecular trapping and investigation of enzymatic activities[3], how pH-responsive polymer brushes can be used for covalent enzyme immobilisation applied on biosensing in complex biofluids[4], and how polymer brushes capable of selective hydrogen bond complexation with polyacids can be used as selective nanosized membrane filters.

2: As the bioanalytical applications of the work in this thesis are varied, this thesis is structured with a small introduction giving a scientific context to each subject separately.

Paper I demonstrates a new method for biomolecular trapping of proteins and enzymes using thermo-responsive polymer brushes in nanoscale chambers. It also demonstrates how enzymes, trapped inside those chambers, retain their enzymatic activity and are able to be used to catalyse cascade reactions, as well as co-factor cycling where a substrate is converted inside the nanochamber, is able to leave, and then be converted again back to the initial state.

Paper II demonstrates an electrochemically stable electrode interface capable of covalently immobilising enzymes in high quantity. While immobilised, the enzymes retain a high activity and are able to catalyse enzymatic breakdown reactions for biosensing purposes, even in complex biofluids such as cerebrospinal fluid.

Polymer brushes 2

A polymer is a large macromolecule whose molecular structure consists of smaller units, known as monomers, covalently bonded together. Once bonded together, these units are no longer known as monomers, but as "repeating units" of the polymer (except for the end-groups). The chain structure of a polymer is constituted of a central backbone, which connects with the other repeating units, and small side chains attached to the backbone that do not interconnect with other side chains. The backbone can be either linear or branched[1], and can contain either just one type of monomer (homopolymers) or several (copolymers). In this thesis the focus is on linear homopolymers that are covalently tethered to surfaces and their behaviour in liquid environments.

1: A branched polymer molecule is composed of a main chain with one or more substituent side chains or branches. However, a branched polymer can also be a polymer that consists of several chains linked together in a central core.

When polymers are tethered with one end to a surface with high enough surface densities the polymer coils are forced to assume a configuration where they extend into solution, forming a hydrated "brush" structure that is significantly larger than the diameter of an isolated coil[5–8]. These nanoscale “polymer brushes” add certain functionality to the structure when it is exposed to a liquid environment. A common use of brushes are for their protein repelling (more commonly referred to as antifouling) properties[9], where the brushes prevent proteins and macromolecules from adsorbing on the surface. However, the wide variety in chemistry[2] between brushes — many of which are responsive to certain external stimuli; including temperature[3], pH[10], ionic strength[11], light[12], and protein[13] or ligand[14] interactions — means that they also find a lot of use as functional materials. This thesis investigates the use of polymer brushes for bioanalytical applications; including brushes for macromolecular gating, brushes as selective diffusion barriers, and brushes as soft scaffolds for biocatalysis and biosensing.

2: The chemical characteristics of a brush is (usually) determined by the single unit side chains attached to the repeating unit of the backbone.

2.1 Polymers on surfaces

There are many ways for a polymer to adsorb on a surface; very much by the same mechanisms any macromolecule would interact with a surface and "stick". However, when we talk about polymer brushes we usually[3] consider polymer chains that are covalently end-grafted to a supporting surface (or interface), meaning that one end of the polymer is stuck to the surface while the other end is not. The structural conformation of the polymers once end-grafted to the surface, and most importantly whether they form a brush or not, is determined by the grafting density Γ, the interactions

3: There is also a type of brush that consist of large branched polymers, where the backbone is physisorbed to a surface while branched chains form a brush structure. These are known as "bottlebrushes"[15].

between the polymer, the surface and the solvent, as well as the average size of the coil. The latter is usually expressed in terms of the polymers radius of gyration (R_g); the average distance from any point in the polymer to its centre of mass[6].

4: $\Gamma \leq R_g^{-2}$

At low grafting densities[4], the polymer coils will be spaced far enough away from each other to not have sufficient interactions to extend into the solution. Instead, the polymers can form into either flat "pancakes" (Figure 2.1A) or swollen "mushrooms" (Figure 2.1B) depending on the degree of interaction with the surface. When the free energy of adsorption (χ_s) of the polymer — the difference in free energy of a repeating unit in the polymer adsorbing on the surface and a solvent molecule adsorbing on the surface — is greater than a certain critical value, the polymer will to maximise the contact area and forms into "pancakes". If the opposite is true, the polymer is entropically repelled from the surface and instead forms into "mushrooms". At high grafting densities[5], the polymer coils will begin to overlap and this forces the polymer to extend into solution to accommodate the additional polymer units; eventually forming a "brush" structure. As the grafting density is increased the polymer will stretch further, reaching a maximum height when then grafting density is the same as the monomer area[6].

5: $\Gamma > R_g^{-2}$

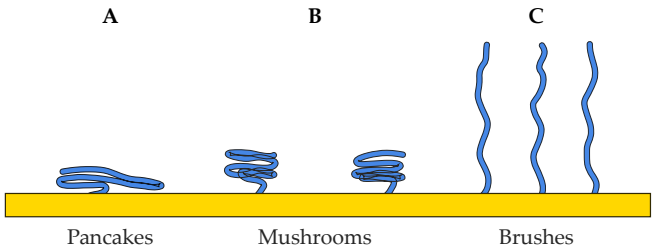

Figure 2.1: Conformations of end-grafted polymers with varying grafting density. (A) The "pancake" conformation exists at low grafting densities when the polymer adsorbs on the surface. (B) The "mushroom" conformation exists at low grafting densities when the polymer is repelled by the surface. (C) The "brush" conformation exists at high grafting densities when the polymers are forced to extend.

In the "mushroom" conformation, the thickness of the end-grafted polymer is approximately the diameter of the coil ($2R_g$), which in turn depends on the degree of interaction between the polymer and the solvent. When the solvent is "good", the coil will swell to maximise contact with the solvent and the height (H) scales with the number of units (N) according to Equation 2.1[6].

$$H = 2R_g \sim N^{\frac{3}{5}} \tag{2.1}$$

When the solvent is "bad", the coil will instead retract into a globule to minimise the contact area with the solvent, and R_g is expected to decrease[6]. A third scenario also exists, when the solvent is on the limit between a good solvent and a bad solvent; known as a "θ" solvent. In this solvent, the swelling will be somewhere in between that of a good solvent and a bad solvent[7][6].

6: $H = 2R_g \sim N^{\frac{1}{3}}$

7: $H = 2R_g \sim N^{\frac{1}{2}}$

When in the "brush" conformation, the thickness of the end-grafted polymer will depend on the size of the coil, the grafting density and the relative interaction of the polymer and the solvent. In a good solvent, the height of the brush will increase linearly with the number of units and scales to the third power with the grafting density. This is known as the Alexander - de Gennes theory, and the height scaling that it gives is shown in Equation 2.2[8].

$$H \sim \Gamma^{\frac{1}{3}} N \tag{2.2}$$

We can further use this relation to derive an expression for the swelling ratio (SR) of the brush. The volume of one polymer coil should be proportional to the number of units, since adding units will make the polymer "bigger", and the height of the stretched polymer should be equal to the volume multiplied with the grafting density (number of chains per area). The height of the brush is given by the Alexander - de Gennes theory. Combining these two yields the swelling ratio as given in Equation 2.3.

$$\mathrm{SR} = \frac{H_{\mathrm{wet}}}{H_{\mathrm{dry}}} \sim \frac{\Gamma^{\frac{1}{3}} N}{\Gamma N} = \Gamma^{-\frac{2}{3}} \tag{2.3}$$

Inverting the swelling ratio gives the volume fraction (ϕ) of repeating units in the brush. While the Alexander - de Gennes theory give a good approximation for the behaviour of an end-grafted polymer in a liquid, it has a limitation in that it assumes that the polymer brush has a sudden transition with a constant volume fraction of $\phi = \phi_0$ when $z \leq H$ to $\phi = 0$ when $z > H$. This has since been disproven, and it has been shown that the volume fraction rather has a parabolic distribution where there is a higher density of polymer closer to the surface[16]. This impacts the interfacial properties of the brush as there is non-uniform solvent penetration and since polymer-polymer interactions are more frequent closer to the surface. Also, the exterior of the brush, which is what macromolecules will come into contact with, will have a lower volume fraction of repeating units compared to deeper in the brush. This might limit the antifouling properties of the brush against small macromolecules, allowing them to enter the brush[8].

8: This is also what I have observed experimentally (Figure 6.5).

2.1.1 Antifouling surface coatings

Brushes are widely used for their ability to prevent non-specific adsorption of macromolecules on the surfaces that they are tethered to. The exact mechanism behind the strong antifouling abilities of (neutral) polymer brushes is debated, but a leading theory is the water barrier theory. It proposes that macromolecules are unable to adsorb on the brush due to a layer of tightly bound water molecules

coordinated to the polymer chains. When a macromolecule adsorbs on the brush, the water molecules that are associated with the brush will be released and the brush will be compressed. The loss of favourable interactions between the coordinated water and the brush, due to the dehydration, and the decrease in entropy of the brush as it is compressed, and it needs to accommodate the volume of the macromolecule, disfavours adsorption. While the release of the water molecules will increase the entropy, this is usually not a strong enough contribution to make the adsorption thermodynamically favourable; that is, as long as the free energy of the brush-water system is increased when the macromolecules adsorbs on the brush it will be expelled from the brush[17–19]. It can be seen as a continuation of the "steric repulsion" theory first proposed by de Gennes. In this model, the steric repulsion resulting from the compression of the brush as the macromolecule adsorbed was the mechanism of the antifouling properties[20].

The water barrier theory should be viable for all polymer brushes that are highly hydrophilic and have an overall neutral[9] electrical charge[21, 22], and the stronger the polymer is able to interact with the interfacial water molecules the better the antifouling ability should be[22]. In fact, it is believed that the excellent antifouling properties of many zwitterionic brushes arise from the fact that the water molecules are even more strongly coupled to the brush through charge-dipole interactions[22, 23]; increasing the barrier for adsorption to be favourable even further. Hydrophobic brushes, which do not interact well with water, are less antifouling[22].

9: Charged brushes, by nature, will electrostatically interact with macromolecules with the opposite charge; reducing their antifouling abilities.

2.2 Grafting polymer brushes

In general, there are three ways to attach polymers to a surface, and two of these allow for end-grafting of the polymer. It is possible to graft a polymer brush from a polymer in solution either via physisorption or with covalent attachment via a functional group on the polymer than can bind to the surface, preferable at the end-terminal of the polymer. The latter is referred to as *grafting-to* and it is usually simple to use and it offers complete control of the molecular weight and polydispersity of the polymer brush, which determines the brushes thickness and homogeneity. However, the technique is limited to polymers that have end-terminals that are available to bind, that is, that are not buried within the polymer coil, and due to steric hindrance during the grafting process the grafting densities achieved are generally quite low. This limits the brushes ability to enter into the "strongly stretched" regime[8].

The third way, and the one used in this thesis, is to graft a polymer brush directly from initiation sites attached to the surface. This is referred to as *grafting-from* and allows for denser and thicker brushes than grafting-to brushes as the grafting is not limited by steric hindrance to the same degree[8]. That is, monomers have the same access to reactive groups throughout the reaction, which allows the growth to continue for long durations, and the initiator layer from which the polymerisation is started can be made very dense, thus increasing the density of the brush. Figure 2.2 illustrates the grafting-from technique of making polymer brushes.

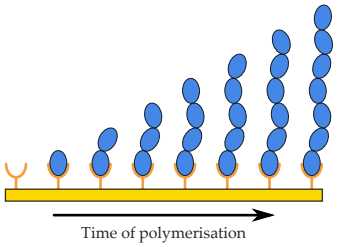

Figure 2.2: Grafting-from technique of making polymer brushes.

The grafting-from technique is based on the growth of polymer chains from the surface using a controlled radical polymerisation (CRP). In CRP, the control comes from a dynamic equilibrium[10] with a small minority of active (radical) species ($P_n^{\bullet}$) and a large majority of dormant species (P_n–X)[11]. Therefore, the rate of activation (k_{act}) must always be slower than the rate of deactivation (k_{deact}) to ensure that the controlled conditions are maintained. The faster deactivation slows down the rate of propagation (k_p), since most active species usually only undergo a single or a few additions of monomer units before converting back to a dormant state, which ensures a homogeneous molecular weight distribution. Having a low number of active species at a given time also slows down the rate of termination (k_t)[12] as the probability that two dormant chains are activated next to one another on the surface is low. Only if deactivated, not terminated, can the dormant species be converted back into an active state to continue the polymerisation[24–26]. A general CRP mechanism is shown in Figure 2.3.

10: Dynamic equilibria are sensitive to external changes in temperature or the removal of reagent, etc.

11: X is a halogen atom. Removal of this atom will activate the dormant species and generate a radical.

12: In polymerisations, propagation is the stage in which a polymer increases its chain length and termination is the stage that ceases the formation of reactive intermediates in the propagation; ending the reaction.

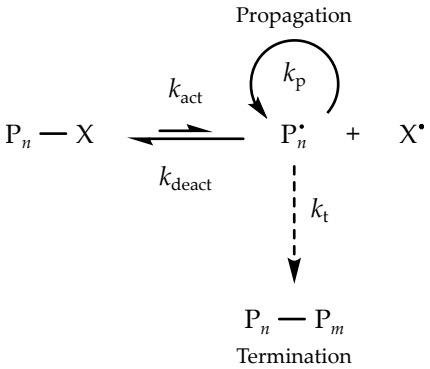

Figure 2.3: General CRP mechanism. A polymer or surface-tethered initiator is activated by external stimuli and is turned into a radical, at which point atoms will be transferred to the growing chain until deactivation or termination of the chain occurs.

Activation and generation of radicals in a CRP can occur by many different means; via spontaneous thermal processes[27, 28], via reversible redox reactions[25, 29], or via reversible chain-transfer processes[30, 31]. This thesis will treat the second of these cases; and more specifically, the mechanism of atom transfer[13] radical polymerisation (ATRP). In ATRP, the active species are generated through a reversible redox reaction catalysed by a transition metal

13: From a mechanistic view, ATRP is closely related to radical addition of alkyl halides across unsaturated C-C bonds; known as atom transfer radical addition; thus, the name.

complex (Mt^n/L), where "L" is a ligand that binds in a complex with the transition metal. This transition metal complex is the catalyst of the ATRP, and will be called the "activator" in its reduced state (Mt^n/L) and the "deactivator" in its oxidised state (Mt^{n+1}/L); in this thesis the transition metal used is copper, and it changes from Cu(I) to Cu(II) in the polymerisation. Termination of the polymer will leave the transition metal complex in an oxidised state and this will eventually deplete the activator; stopping the reaction. The ATRP mechanism is shown in Figure 2.4.

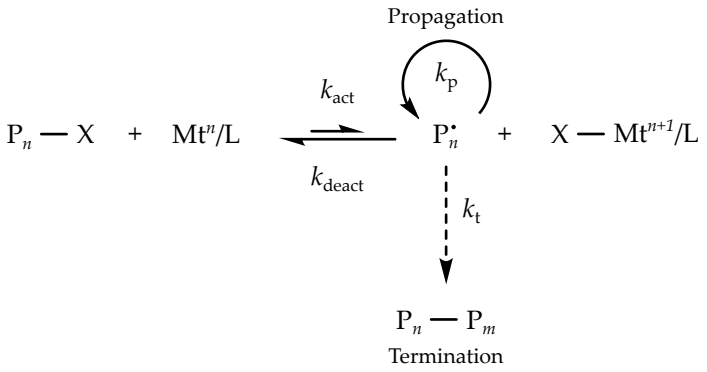

Figure 2.4: ATRP mechanism. Activation of the dormant species is done via a reversible redox reaction with a transition metal complex, which is oxidised in the process.

While ATRP is widely used in both academic studies and industry, it has two big limitations; the first of which is the sensitivity of the transition metal complexes to air (oxygen). This can be overcome by starting with the transition metal in its oxidised state (Mt^{n+1}/L) and then reduce it, using a reducing agent such as ascorbic acid[32], to initiate the polymerisation, effectively eliminating the oxygen sensitivity during the preparation stage[33]. As long as the amount of oxygen in the solution during the polymerisation itself is kept a minimum, the reaction should proceed as ATRP. This mechanism is called activators generated by electron transfer (AGET).

The second issue of ATRP lies in the large amounts of metal catalyst required to propagate the polymerisation for extended durations; leaving large amounts of residual metals in the finished polymer that requires difficult purification[34]. However, since ATRP is controlled by a dynamic equilibrium, it is not the total concentration of catalyst that determines the polymerisation rate (R_p); it is the ratio of activators and deactivators. Therefore, lowering the total concentration of the transition metal complex should not have an impact on R_p[35]. However, while it is tempting to just lower the concentration, the unavoidable terminations will irreversibly consume the activator and eventually stop the reaction.

By combining the concepts of AGET ATRP, with a reducing agent capable of generating activators from deactivators in high excess, and lowering the total concentration of the transition metal complex to parts-per-million (ppm) concentrations it is possible to achieve a controlled reaction which yields low polydispersive polymers,

on surfaces, that is less sensitive to air (oxygen) than regular ATRP. Since the reducing agent is now not only generating the activator, but effectively regenerating it since it also takes into consideration termination and the presence of air and other radicals in the system, this technique is called activators regenerated by electron transfer (ARGET)[35]. The ARGET mechanism is shown in Figure 2.5.

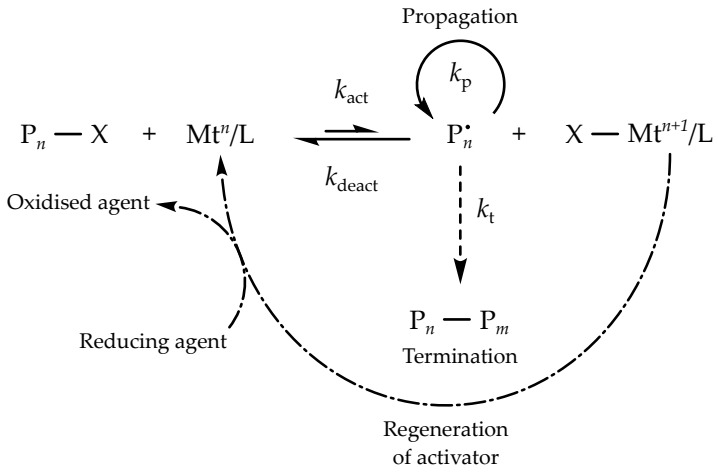

Figure 2.5: ARGET ATRP mechanism. Regeneration of the activator is done via an electron transfer to the deactivator from a reducing agent.

2.2.1 Kinetics of ATRP

As mentioned earlier, ATRP relies on establishing an equilibrium between a halogenated dormant species (P_n−X) and active species ($P_n^\bullet$) that are produced by cleaving the C−X bond with an activator (Mt^n/L), creating a deactivator (X−Mt^{n+1}/L) in the process. The rate of ATRP (R_p) is determined by the rate of propagation (k_p), the monomer concentration ([M]) and the concentration of radicals ($[P_n^\bullet]$) active in the system[26][14], as shown in Equation 2.4.

14: This is the kinetics of a second order (or bimolecular) reaction.

$$R_p = k_p [P_n^\bullet] [M] \tag{2.4}$$

At the ATRP equilibrium, the equilibrium constant of the activation/deactivation cycle K_{ATRP} will be proportional to the activation (k_{act}) and deactivation (k_{deact}) constants[15]. An equilibrium constant will also be proportional to the concentrations of the products and reactants in the reaction[16]. We can simplify the expression in Equation 2.4 by substituting the concentration of radicals ($[P_n^\bullet]$) by combining the two equilibrium constants expressions. This gives the "ATRP equation"[26], as shown in Equation 2.5.

15: $K_{ATRP} = \frac{k_{act}}{k_{deact}}$

16: $K_{ATRP} = \frac{[P_n^\bullet][X{-}Mt^{n1+}/L]}{[P_n{-}X][Mt^n/L]}$

$$R_p = k_p \left(\frac{k_{act}}{k_{deact}}\right) \left(\frac{[Mt^n/L]}{[X - Mt^{n1+}/L]}\right) [P_n - X] [M] \tag{2.5}$$

At the ATRP equilibrium, the rate of ATRP is determined by (1) the rate of propagation (k_p), (2) the monomer concentration ([M]),

(3) the ratio of activation/deactivation constants, (4) the ratio of activator/deactivator concentrations and (5) the concentration of the dormant species. Each monomer has its own intrinsic rate of propagation that cannot be changed[17], and the concentration of the dormant species is determined by the number of initiator sites at the start of the reaction, which will decrease as termination of the polymer chains occur. Therefore, these two parameters are hard to vary. That leaves (2), (3) and (4), as shown in Equation 2.6, as viable parameters to change in order to optimise an ATRP protocol.

17: This has to do with the reactivity of the monomer and the active species, which is determined by the molecular structure of the two.

$$R_\mathrm{p} \propto \left(\frac{k_\mathrm{act}}{k_\mathrm{deact}}\right)\left(\frac{[\mathrm{Mt}^n/\mathrm{L}]}{\left[\mathrm{X}-\mathrm{Mt}^{n1+}/\mathrm{L}\right]}\right)[\mathrm{M}] \tag{2.6}$$

The rate of ATRP can be directly increased or decreased by changing the monomer concentration, making this an easy parameter to change when optimising ATRP. The ratio of the rates of activation and deactivation can be adjusted by changing the reactivity of the transition metal complex, or more specifically its ligand structure, towards the dormant species (k_act) and towards the active species (k_deact). This ratio is determined by the bond dissociation energy of the C−X bond compared to the strength of the Mt^{n+1}−X bond or the halogenophilicity[18] of Mt^n; a stronger C−X bond will decrease k_act and lower the ratio, and vice versa. In the case of Cu(I)/Cu(II), C−Br is considered to give the highest reactivity, followed by C−Cl and at the slowest C−I. The halogenophilicity of Mt^n/L complex can be varied by exchanging the ligand, which will effect the redox potential of the Mt^n/L-Mt^{n+1}/L couple and bond strength of X−Mt^{n+1}/L. As a rule of thumb, the more reducing the metal-ligand complex is, which increases with electron-donation from the ligand, the activity will increase[36, 37]. The ligands I have used[19] are ranked, based on ATRP activity, accordingly[37]:

18: Halogenophilicity describes the ability of a nucleophile to "attack" a halogen in a substitution reaction.

19: Tris[2-(dimethylamino)ethyl]amine ($\mathrm{Me_6}$TREN), N,N,N,N,N-pentamethyldiethylenetriamine (PMDETA) and 2,2′-bipyridine (bpy).

$$\mathrm{Me_6TREN} >> \mathrm{PMDETA} > \mathrm{bpy}$$

The last viable parameter to optimise in Equation 2.6 is the ratio of the concentrations of activator and deactivator in the solution. In ATRP, this ratio will decrease over time as radical termination irreversible converts the transition metal complex to its oxidised state (X−Mt^{n+1}/L). This will in turn slow down — and eventually stop — the polymerisation. However, by reducing the deactivator after termination, as in ARGET ATRP, the ratio can be kept constant. Further, by controlling the reduction of the deactivator via different reducing agents, temperature, or by slowly feeding the reducing agent[38], the rate of ATRP can be controlled[37].

Finally, while not a direct factor, the choice of solvent in the reaction has been shown to affect the rate of ATRP; especially more polar solvents have been observed to give higher equilibrium constants.

This is believed to be due to stabilisation of the more polar oxidised state ($X{-}Mt^{n+1}/L$) of the transition metal complex, compared to the less polar reduced state (Mt^n/L)[37]. Water is especially good at generating high ATRP activation; at the cost of generating a lot of radicals and a high resulting rate of termination[39]. The solvents I have used are ranked, based on ATRP activity, accordingly[37]:

$$\text{Water} >> \text{DMSO} > \text{Methanol} > \text{Toluene}$$

2.2.2 Termination in ATRP

Termination is unavoidable in ATRP systems because of the very nature of radicals. This is equally true on surfaces as it is in solution. However, the modes of termination might differ. It is believed that termination in ATRP mainly occurs through radical coupling, that is, that two active chains connect and thus "close the loop" in the brush, as well as through radical disproportionation[20], meaning that two radicals interact, but instead of coupling one of the radicals donates a hydrogen atom (usually from the β-position) to the other. The polymers are considered "dead", but are not connected[36].

20: Disproportionation in ATRP can also refer to the redox exchange with two Mt^n complexes combining into Mt^{n+1} and Mt^{n-1}, which is favoured especially in more polar solvents[37]. However, in most ATRP, the concentration of Mt^n is too low for this to impact the rate of ATRP[36].

In solution, termination can occur by two active chains diffusing in the solution connecting and, by coupling or disproportionation, terminating the radical. However, polymer brushes are tethered; restricting their mobility and ability to move and connect with other radicals considerably[40]. Simulations of surface-initiated ATRP has suggested a mechanism of "migrating radicals"[21] as a means of both the growth of the polymer brush as well as the primary means of termination. That is, instead of considering individual chains as activating, attaching a few monomers, and then deactivating in the reaction, it is radicals that are moving from chain to chain. When two radicals move to adjacent chains there is a chance of termination occurring[41]. This mechanism explains the connection between the rate of activation and deactivation in ATRP and the rate of termination; more active radicals migrating on the surface will increase the probability of two of them moving adjacent to one another. As the polymer chains grows the brush is known to become less dense[16], and this too could be linked to a decrease in termination as the distance between the migrating radicals increase; despite the increase in flexibility of the chains.

21: Radicals "jump" from an active chain to a dormant chain through the activation/deactivation cycle. It is explained in detail in the works by Zhou[40] and Gao[41].

Important to this work, with respect to ATRP done with nanopores, is the geometric dependency on the termination. On a concave surface, the brushes are in a more confined environment than on a flat surface; leading to closer proximity of the chains[42]. This will increase the probability of termination, as the radicals are formed in a denser environment. In the case of a pore, this could effectively "close" it if termination happens through coupling.

Methodology 3

In no particular order, this chapter will briefly cover the surface sensitive techniques, optical techniques and electrochemical techniques that I have used throughout this thesis work. It will also cover the procedures I used for synthesis of polymer brushes, as well as the initiator layer synthesis and assembly.

3.1 Surface sensitive techniques

3.1.1 Surface plasmon resonance

Surface plasmon resonance (SPR) sensing is a refractometric (optical) label-free technique that is used to detect nanoscale (ng/cm^2) adsorption events, both covalent and non-covalent, of an analyte in the vicinity of a sensor surface. It does this by measuring the change in the incident angle required to excite surface plasmons, propagating waves of electrons that are able to form on certain metallic thin films under certain conditions. Plasmons are generated when plane-polarized light impinge the thin metal film under total internal reflection conditions[1] when passing from a dense medium (a glass prism) into a less dense medium (air or water). At, and above, the TIR angle no light will exit the prism, but the electric field of the photons will extend out beyond the interface. When that interface has available electrons, such as when there is a film of gold on the surface, and when the wave vector of that electric field matches the plasmons wave vector, a plasmon will be generated; leading to rapid decrease in the intensity of reflected light due to absorption by the plasmons[43, 44].

1: When light passes from a medium to a less dense medium the light will be bent towards the plane of interface. Increasing the incident angle enough will make all incoming light reflect at the interface; this is called total internal reflection (TIR).

Figure 3.1 demonstrates a typical angular reflectivity spectrum in air. As mass adsorbs on the thin film the refractive index close to the surface changes, and this will in turn shift the incident angle of light required to reach the SPR minimum (Figure 3.1B) to higher angles. If there is also a significant change in the refractive index of the bulk solution (or air) the TIR (Figure 3.1A) will also shift to higher incident angles. Tracking the shift in incident angle of TIR and SPR over time allows kinetics and magnitudes of the adsorptions to be determined and are usually plotted in a "sensorgram".

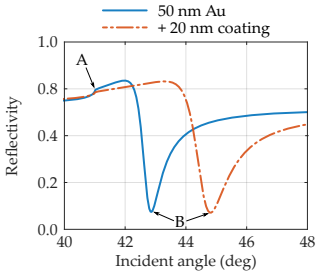

Figure 3.1: Angular reflectivity spectrum for a $\lambda = 670$ nm light source impinging on a 50 nm gold thin film in air, with and without a 20 nm thin coating ($n = 1.4$). (A) TIR angle. (B) SPR minimum angle.

As mentioned earlier, SPR measures adsorption events of an analyte in the vicinity of a sensor surface. However, it does not only measure molecules that attach to the surface; at high enough concentrations it measures everything within the decay length of the electric field of the surface plasmons. This distance away from the surface

that an adsorption event occurs determines the sensitivity of the technique. Adsorption events that occur far away from the surface will lead to smaller shifts in the incident angle, which is important to keep in mind when performing measurements on brushes on the scale of 100s of nm. As a rule of thumb, the effective "probe depth" of SPR is approximately 37% of the incident lights wavelength[45]. A more accurate estimation derived from Maxwell's equations is shown in Equation 3.1[46], where λ is the wavelength of the incident light, η_d is the refractive index of the bulk phase and ε'_m is the real part of the dielectric constant of the metal.

$$\delta \approx \frac{\lambda}{2\pi}\sqrt{\left(\frac{\eta_d^2 + \varepsilon'_m}{\eta_d^4}\right)} \tag{3.1}$$

Quantitative information from the angular reflectivity spectrum can be extracted with Fresnel models. Simply, these are equations (formulated from Maxwell's equations of electromagnetism) that describe how the incident light waves interact with different materials by propagation, reflection, absorption or scattering. Solving these equations will extract the thickness and refractive index of an adsorbed layer, as long as all but one of the parameters are known[47][2]. When it comes to hydrated polymer brushes, direct modelling of the thickness is not possible; mainly due to the unknown degree of hydration, which will impact the effective refractive index of the adsorbed layer. Instead, a non-interactive probe needs to be used to estimate the intrinsic exclusion volume away from the surface; which should correspond to the wet height of the polymer brush. By comparing the TIR and SPR response with, and without, the non-interactive probe in combination with the Fresnel equations makes it possible to extract the thickness and effective refractive index of a hydrated layer from a sensorgram. This method was first developed by Schoch et al.[46] and then further refined by Emilsson et al.[48] with the incorporations of the Fresnel equations, which eliminated the need to estimate the "effective" decay length of the evanescent field. Further work by Svirelis et al.[49] has expanded the concept of the non-interactive probe for use in bulk-correction when doing high concentration injections on hydrated polymer films, which by comparing the SPR and TIR response of a non-interactive probe allows us to determine how much of the SPR response was from interactions with the surface and how much was from the analytes simply occupying volume close to the surface. This method was used for the kinetics determinations in the unpublished results on NPC mimics.

2: A detailed description of the Fresnel equations can be found in the book "Plasmonic biosensors: an integrated view of refractometric detection" by A. Dahlin[47].

3.1.2 Quartz crystal microbalance with dissipation

Quartz crystal microbalance with dissipation (QCM-D) is an gravimetric label-free technique that is used to detect nanoscale (ng/cm^2) adsorption events, both covalent and non-covalent, of an analyte that attach to, or couples with, a sensor surface. This is done by measuring the resonance frequency of the oscillation's odd overtones[3], which are determined by the mechanical properties of the crystal and the medium that is oscillates in. Whenever an event occurs that changes these properties, such as absorption of mass to the surface, the resonance frequency will shift either to lower values (mass added) or higher values (mass removed). However, the relationship between adsorbed mass and frequency only holds true for dry and rigid systems. In liquid environment, more often than not, water will be coupled to the surface whenever an analyte binds. Water, being highly viscous, will result in an adsorbed film that is not fully coupled to the resonance, which in turn will lead to dampening of the oscillation; that is, energy is lost[51, 52].

3: When the overtone is odd there will be an antisymmetric deformation in the wave going through the crystal, and this will generate a measurable current as quartz crystal is a piezoelectric material. However, if the overtone instead is even, the deformation will be symmetric and no current is generated[50].

We can define the energy dissipation as the ratio of energy lost per oscillation cycle ($E_{\text{dissipated}}$) and the amount of energy stored in the system (E_{stored}), as shown in Equation 3.2.

$$D = \frac{1}{2\pi}\left(\frac{E_{\text{dissipated}}}{E_{\text{stored}}}\right) \tag{3.2}$$

Energy dissipation can be monitored by exciting an oscillation with a short voltage pulse, and then measuring the oscillation decay over time after the pulse is turned off. Tracking how the energy dissipation and the frequency shift varies over time molecular interactions and changes in surface properties, such as its rigidity, can be determined, as demonstrated in Figure 3.2. When an event occurs on the surface that changes the viscoelastic properties of the adsorbed layer on the surface, the energy dissipation with shift to either lower values (more rigid) or higher values (more viscous).

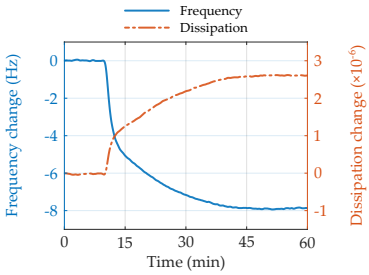

Figure 3.2: QCM-D time trace with frequency and dissipation changes measured at the 3rd overtone.

Usually the 3rd or the 5th overtone[4] is used in quantitative analysis of QCM-D measurements. However, similarly to SPR where the incident light wavelength affects the probing depth, changing the overtone will change the viscous penetration depth[5] generated by the oscillation. Higher overtones will have shorter penetration depths, allowing events at different positions in a hydrated film to be observed simultaneously. The penetration depth (Δ_n) can be estimated with Equation 3.3[53], where ρ_m is the density of the adsorbed film, η_m is the viscosity of the adsorbed film, f_0 is the fundamental frequency, and n is the overtone.

$$\Delta_n = \sqrt{\frac{1}{\pi n f_0}\left(\frac{\eta_m}{\rho_m}\right)} \tag{3.3}$$

4: The sensing area of the overtones decreases towards the centre while the mass sensitivity increases as a bell shape with the highest sensitivity in the centre of the crystal[53].

5: When in a viscous medium, the oscillations of the crystal will couple to the medium and transfer into the bulk. The transferred motion will be an induced, highly damped, sinusoidal shear wave that travels away from the sensor surface. The decay constant of the the shear wave is the effective penetration depth[51, 53].

Equation 3.3 can be used to estimate the penetration depth. However, due to the parabolic distribution of polymer in a brush[16], the viscosity to density ratio of the hydrated film will not remain the same throughout the entire shear wave. Where the monomer concentration of polymer is high, the viscosity to density ratio will also be high, as polymers in general have a much higher viscosity as water, while having a similar density. As the water content increases further away from the surface, the viscosity to density ratio will decrease and so will the effective penetration depth relative to that distance away from the surface. The general progression, where higher overtones have lower penetration depths, should still hold true despite the nonideal shear wave in the film.

3.2 Experimental

3.2.1 Absorbance measurements

Absorbance measurements were performed with a fibre coupled array spectrometer and lamp (BH-2000-BAL Deuterium-Halogen Light Source, Ocean Optics) with collimating lenses[54].

In paper I, the conversion of NAD^+ to NADH was studied in-situ my monitoring the absorbance of light around 340 nm. A peristaltic pump was used to direct flow through the flow cell.

In paper II, the FOX assay[6] was used to quantify the production of H_2O_2 by the enzymes. The assay was prepared by mixing 0.5 mL of 25 mM ammonium ferrous (II) sulfate composition in 2.5 M H_2SO_4 with 50 mL of 100 mM sorbitol and 125 μM xylenol orange (*o*-cresol-sulfonephthalein-3´-3´-bis-[methyliminodiacetic acid sodium salt])) in water, and 2 mL of mixture was added to a vial containing 0.2 mL sample with H_2O_2. The sample was incubated for 20 min at room temperature before quantification to ensure complete conversion and measured at 580 nm.

6: The assay is named after the main reaction that occurs; the ferrous oxidation of xylenol orange[55].

3.2.2 Fluorescence microscopy

Fluorescence measurements were performed using an inverted Axio Observer optical microscope equipped with an Andor IXon Life CCD and an Axiocam color camera, LED light sources and a 50× objective (air, NA = 0.55, WD = 9.0 mm) in epi-mode.

In paper I, the presence of modified GOX-Cy3 and GAL-FITC was verified with excitation at 511 nm and emission filtered between 585-620 nm (Cy3) and excitation at 478 nm and emission filtered between 525-550 nm (FITC). The conversion of resorufin in the

presence of H_2O_2 (Figure 4.7A) was monitored with excitation at 555 nm and emission between 565 and 605 nm.

In the unpublished results, the transport of Cy3-modified PMAA was monitored with excitation at 511 nm and emission filtered between 585-620 nm and the FITC-modified PMAA monitored with excitation at 478 nm and emission between 525-550 nm.

3.2.3 Infrared spectroscopy

Fourier transfer infrared spectroscopy (FTIR) measurements were performed using a Perkin Elmer FT-IR Spectrometer. Spectra were measured in the mid-infrared region (4000-400 cm^{-1}) and FTIR spectra with analysis for the polymer brushes worked with in this thesis are found in Appendix A.1, A.2 and A.3.

3.2.4 Cyclic voltammetry

Cyclic voltammetry (CV) was performed with the Reference 600+ (Gamry Instruments) potentiostat; a conventional three-electrode setup was used, with the gold substrate as the working electrode, a platinum wire mesh as counter electrode, and a Ag/AgCl electrode as reference. Measurements were performed with 1 mM ferrocene-methanol in a 150 mM PBS solution (pH 7.5) unless otherwise noted. CV was used to determine the standard redox potential (E_0) of the redox probe as the average of potential values at which the cathodic and anodic current maxima. All CV sweeps were initiated with an anodic sweep from -0,2 V to +0,5 V, followed by a cathodic sweep from +0.5 V to -0.2 V, at 10 mV/s, 25 mV/s, 40 mV/s, 60 mV/s, 90 mV/s, 160 mV/s, 250 mV/s and 360 mV/s. Five cycles were run and the average of the last three were used to determine the cathodic and anodic current maxima as well for the diffusional analysis. Open current potential (OCP) was checked to verify electrode stability before each measurement was run.

Diffusional analysis was performed with the Randles-Ševčík equation (Equation 3.4), which describes the effect of scan rate (v) on the peak current (i_p) for a cyclic voltammetry experiment. According to the equation, when cathodic (or anodic) peak is linear with the square root of the scan rate the electrochemical process is diffusion controlled and the slope of the line should be proportional to the square root of the effective diffusion coefficient (D) of the analyte undergoing a redox reaction at the electrode[56]. Analysis was done with MatLab.

$$i_p = \left(0.4463nFCA_{\text{eff}}\sqrt{\frac{nFD}{RT}}\right)\sqrt{v} \tag{3.4}$$

3.2.5 Impedance spectroscopy

Electrochemical impedance spectroscopy was performed with the Reference 600+ (Gamry Instruments) potentiostat; a conventional three-electrode setup was used, with the gold substrate as the working electrode, a platinum wire mesh as counter electrode, and a Ag/AgCl electrode as reference. Measurements were performed with 1 mM ferrocenemethanol in a 150 mM PBS solution (pH 7.5) unless otherwise noted. All EIS measurements were performed with a DC potential set at the E_0 of ferrocenemethanol over frequencies ranging from 10^4 to 10^{-1} Hz, with an AC amplitude of 5 mV. Three repeats were run, and the average of these was used for equivalent circuit fitting with a modified Randles circuit.

The modified Randles circuit used in the equivalent circuit fitting was based on a model for polymer brushes suggested by Anthi et al.[57], and is shown in Figure 3.3. It consists of the solution resistance (R_s) in series with a resistance of the brush (R_p) and capacitance of the brush (C_p). These elements mimic the migration of charges through the structure of the brush (R_p), which reflects its penetrability for ions, and the polarization of electric dipoles in the brushes (C_p), which reflects its dielectric permittivity[57]. The brush is then in series with a Randles equivalent circuit[56], which consists of a charge transfer resistance (R_{ct}), a double-layer capacitance (C_{dl}) and a Warburg[7] element (Z_w). These elements mimic the electron transfer between analyte and electrode (R_{ct}), the charging of the interfacial electric double-layer of the electrode surface (C_{dl}) and the diffusion limit at low frequencies (Z_w). The Warburg element is a solution to Fick's equation of mass transfer and is a part of the interfacial impedance[58]. Initial fitting was done in the Gamry Instruments software and final analysis was done with MatLab.

7: Named after the German physicist Emil Warburg, who did research on electrochemical ion transport processes in the late 1800s.

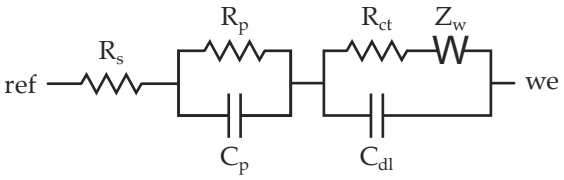

Figure 3.3: Equivalent circuit used for EIS analysis in paper II.

3.2.6 Chronoamperometry

Amperometry measurements were performed with the Reference 600+ (Gamry Instruments) potentiostat; a conventional three-electrode setup was used, with the gold substrate as the working electrode, a platinum wire mesh as counter electrode, and a Ag/AgCl electrode as reference. Chronoamperometry was measured at -0.7 V. CV was run on each electrode before use to ensure

solvent availability. All analytes were introduced in PBS at pH 7.5. The measurements done in cerebrospinal fluid (CSF) were done in the same conditions, but with 10× diluted CSF instead of pure PBS buffer. Charge transfer densities were determined by measuring amperometry and integrating during 25 s, ignoring the first 5 s when the potential is established. Charge transfer densities for H_2O_2 was determined for several concentrations between 0.01 mM and 1 mM for electrode availability analysis.

Electrode availability analysis was performed with the integrated Cottrell equation (Equation 3.5). The Cottrell equation describes the change in electric current (i_p) with respect to time (t) after a potential step is applied over the electrochemical cell. In its integrated form[8], it shows that the charge transfer density (Q) should be linear with the square root of the time for the electrochemical process to be diffusion controlled and the slope of the line should be proportional to the square root of the diffusion coefficient (D) of the analyte undergoing a redox reaction at the electrode[59].

8: In this form the equation is also known as the Anson equation, after Fred Anson, who applied the integrated Cottrell equation on processes with surface adsorption[59].

$$Q = \left(2nFA_{\text{eff}}C\sqrt{\frac{D}{\pi}}\right)\sqrt{t} \tag{3.5}$$

Given that the diffusion coefficient is known, the integrated Cottrell equation can also be used to determine the concentration of the reacting analyte, which can be useful for biosensing applications.

3.3 Polymer brush synthesis

3.3.1 Surface cleaning

Gold-coated SPR and QCM-D sensor surfaces were washed in TL1 solution (5:1:1 v/v of $H_2O/H_2O_2/NH_4OH$ at 75°C) for 20 minutes. This was followed by rinsing in MQ water, then ethanol, then sonication (35 kHz) for 1 minute and then dried with N_2 before further treatment. Had the surfaces been used previously, an initial wash was done in Piranha solution (3:1 v/v of H_2SO_4/H_2O_2) for 20 minutes, followed by rinsing in MQ water and then as normal.

Gold-coated nanopore substrates, with and without the chamber, were etched in NaOH (10 mM) to remove the protective aluminium oxide coating[9]. This was followed by washing in TL1 solution (5:1:1 v/v of $H_2O/H_2O_2/NH_4OH$ at 75°C) for 20 minutes, rinsing in MQ water, then ethanol and then dried with N_2 before further treatment. *Ultrasonication has a high risk of breaking the delicate membranes of the nanopore substrates and should be avoided!*

9: More information can be found in the paper by Malekian et al.[60]

3.3.2 Thiol initiator layer

In paper I, and in the unpublished results, 11-mercaptoundecyl-2-bromo-2-methylpropanoate[10] (MuBB) was used as the initiating anchor layer attached to the gold from which ATRP was performed. α-bromobutyrate-11-undecanethiol (BrUDT) was also used in paper I. However, as bromines on tertiary carbons are known to be more active than bromines on primary carbons[37], MuBB should be the better candidate for ATRP despite the slight increase in steric hindrance from the additional ester and methyl groups[11].

10: ω-mercaptoundecyl bromoiso - butyrate is another name for it.

11: Note that this is only relevant for the very early stages of ATRP, once the brush begins to form it will be the chemistry of the monomer that determines the activation rate; that is, the unit carrying the halide.

Cleaned surfaces were immersed in initiator solution (2 mM MuBB in anhydrous ethanol). The substrates were exposed for 12–18 hours. After self-assembly, the substrates were thoroughly rinsed in ethanol, sonicated (35 kHz) in ethanol for 1 minute and then dried with N_2. Samples were used immediately.

3.3.3 Diazonium initiator layer

Synthesis and deposition of PEBrMP consists of three steps; (1) diazonium synthesis, (2) radical formation, followed by surface deposition, and (3) bromination of the alcohol. These steps are shown in Figures 3.4-3.6.

In paper II, 4-(phenethyl 2-bromo-2-methylpropanoate) (PEBrMP) was used as the initiating anchor layer attached to the gold from which ATRP was performed. Unlike MuBB and BrUDT, PEBrMP is a derivative from a diazonium salt. These molecules can strongly, and covalently, attach to the surface and are known to be electrochemically stable[61], making it ideal for the electrode interface.

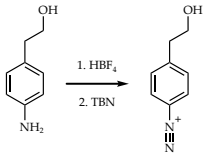

Figure 3.4: PEBrMP synthesis, 1.

4-Aminophenethyl alcohol (0.22 g, 1.60 mmol) was diluted with MQ water (1 mL) and protonated with HBF_4 (0.3 mL, 48%). The solution was cooled in an ice bath and tert-butyl nitrite (0.2 mL, 1.70 mmol) was added dropwise while stirring. The solution was left to stir for 1 h until 4-aminophenethyl alcohol was fully converted into 4-(2-hydroxyethyl)phenyldiazonium tetrafluoroborate.

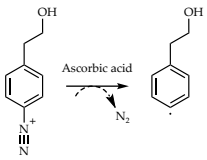

Figure 3.5: PEBrMP synthesis, 2.

Simultaneously, using a separate flask, ascorbic acid (0.035 g, 0.20 mmol) was dissolved in MQ water (50 mL) and the solution was deoxygenated with N_2 for 1 h. Then, the ascorbic acid solution was transferred into a sealed glass jar with cleaned surfaces. The diazonium salt was deoxygenated with N_2 for 5 min and transferred to the jar via needle. Cleaned surfaces were exposed to the diazonium salt for 1 h and then rinsed with MQ water and ethanol and dried under flow of N_2.

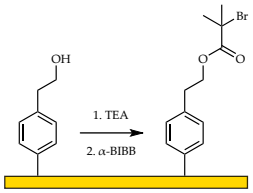

Figure 3.6: PEBrMP synthesis, 3.

To convert the diazonium salt into PEBrMP, the surfaces were allowed to equilibriate in dichloromethane for 1 minute and then exposed to α-bromoisobutyryl bromide (0.500 mL, 4.05 mmol) and triethylamine (0.675 mL, 4.84 mmol) in dichloromethane (50 mL) for 15 min, after which surfaces were rinsed in ethanol and dried under flow of N_2. Samples were used immediately.

3.3.4 ARGET ATRP of PAA

ARGET ATRP of PAA (Figure 3.7) on PEBrMP.

$CuCl_2$ (0.0053 g, 0.04 mmol), and PMDETA[12] (0.065 mL, 0.31 mmol) were dissolved in dimethyl sulfoxide (20 mL). Toluene (12 ml) and tert-butyl acrylate (10 ml, 68.00 mmol) were added, and the solution was deoxygenated with N_2 for 1 h.

The reaction solution was then transferred via cannula into a screw-top jar (with rubber septa lid) containing initiator-prepared gold surfaces. The reaction was initiated by the addition of L-ascorbic acid (0.045 g, 0.26 mmol) and was quenched after 30 min by immersing the surfaces in ethanol. To convert the poly(tert-butyl acrylate) brushes into PAA brushes the surfaces were exposed to methanesulfonic acid (0.300 mL, 4.62 mmol) in dichloromethane (50 mL) for 15 min, after which surfaces were rinsed in ethanol.

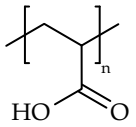

Figure 3.7: PAA (protonated form).

12: N,N,N,N,N-Pentamethyldiethylenetriamine

3.3.5 ARGET ATRP of PHEAA

ARGET ATRP of PHEAA (Figure 3.8) on MuBB.

N-hydroxyethylacrylamide (3.33 g, 28.9 mmol) was dissolved in methanol (30 ml). $CuBr_2$ (0.0025 g, 0.01 mmol), and Me_6TREN[13] (0.305 mL, 0.12 mmol) were dissolved in water (10 mL) and added, and the solution was deoxygenated with N_2 for 1 h.

The reaction solution was then transferred via cannula into a screw-top jar (with rubber septa lid) containing initiator-prepared gold surfaces. The reaction was initiated by the addition of L-ascorbic acid (0.020 g, 0.11 mmol) and was quenched after the allotted reaction time by immersing the surfaces in ethanol.

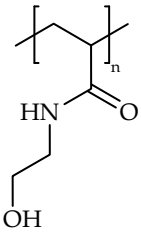

Figure 3.8: PHEAA.

13: Tris[2-(dimethylamino)ethyl]amine

3.3.6 ARGET ATRP of PNIPAM

ARGET ATRP of PNIPAM (Figure 3.9) on MuBB.

N-isopropylacrylamide (2.66 g, 23.5 mmol) was dissolved in methanol (30 ml). $CuBr_2$ (0.0067 g, 0.03 mmol), and PMDETA[14] (0.065 mL, 0.31 mmol) were dissolved in water (19 mL) and added, and the solution was deoxygenated with N_2 for 1 h.

The reaction solution was then transferred via cannula into a screw-top jar (with rubber septa lid) containing initiator-prepared gold surfaces. The reaction was initiated by the addition of L-ascorbic acid (0.086 g, 0.49 mmol) and was quenched after the allotted reaction time by immersing the surfaces in ethanol.

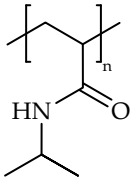

Figure 3.9: PNIPAM.

14: N,N,N,N,N-Pentamethyldiethylenetriamine

Molecular Trapping of Enzymes in Nanoscale Chambers

4

This chapter summarises the first paper presented in this licentiate thesis, "Stable Trapping of Multiple Proteins at Physiological Conditions using Nanoscale Chambers with Macromolecular Gates". It was published in August 2023 in Nature Communications[3].

My main contributions to the paper consisted of (1) using the molecular trapping system to selectively capture the enzymes glucose oxidase (GOX) and β-galactosidase (GAL) in the nanochambers and then verifying that ligand exchange between the nanochamber and its surroundings is possible by investigating the enzymatic conversion of lactose to H_2O_2 in a cascade reaction confined to the nanochambers and confirming that H_2O_2 was able to leave. I also (2) extended this study to investigate cofactor cycling between the nanochambers and the surroundings between the enzymes alcohol dehydrogenase (ADH), GOX and horseradish peroxidase (HRP), which convert the cofactor NAD^+ to NADH, and back.

4.1 Scientific context

Enzymes and other biomolecules tend to exhibit complex dynamic structures with conformational changes that have various lifetimes[1]. While recently there has been an upsurge in new computational methods for predicting these structures in proteins, for instance AplhaFold that uses AI to predict a protein's 3D structure from its amino acid sequence on the atomic scale[62]. Yet, while predictive computational models will most certainly play a large role going forward in advancing our understanding of life on the molecular level, and in predicting completely new structures for biophysical[63, 64] and theraputical[65, 66] studies, computational simulations can never completely replace experimental data[2].

1: These lifetimes are on the scale of nanoseconds to milliseconds, meaning that long-term observations are required to capture the dynamics.

2: Of course, AI should be used in conjunction with experimental data; which confirms any predictions and reveal domain arrangements, while AI provides atomic details[64, 67].

Single-molecule detection and analysis enables us to experimentally observe protein dynamics, their self-interactions (oligomerization and aggregation) or their interactions with other proteins and ligands; even on the scale of a single or a few proteins. With stable and strong fluorescent dyes conjugated to the proteins it is possible to observe these events on a single event level[68]. However, in order to guarantee that only single events are observed, the excitation volume from which light is collected needs to be reduced drastically. This is commonly done with confocal setups, which limits the excitation light to only in-focus light. However, while the small excitation volume is small, so is the time which the protein spends inside that volume; limiting observation time.

The limited observation time can be extended by encapsulating the protein within the confocal excitation volume. A crude way to do this is to directly tether the protein to a surface, for instance by attaching biotin-modified biomolecules to streptavidin-modified surfaces[69]. However, this can limit the conformational freedom[70] and induce changes in the protein structure due to interactions with the surface[71]. In order to truly study proteins in their native state, universal label-free detection is required. Our approach to achieve this is to trap the proteins in small containers. This would both confine the protein for long times and, if the walls are repelling, allow the proteins free diffusional movement within a confined optical detection volume with little interactions with the surface. This has been attempted with soft matter containment, such as within liposomes[70, 72]. However, liposomes have drawbacks in lack of yield; it is difficult to trap many proteins within the vesicle, making studies on protein-protein interaction difficult. Also, the nature of the vesicle limits diffusion of small molecules to cross the membrane to access the protein, making studies on protein-ligand interaction difficult. To achieve long-term measurements of these interactions, a permeable barrier where small molecules, ions and ligands have unhindered access to the protein, is necessary.

4.2 Thermo-responsive gating with PNIPAM

In summary, the main considerations that need to be considered for the biomolecular trapping device is that (1) it has to be able to selectively catch and capture proteins, that (2) the proteins remain trapped for a long duration (at least several minutes), and that (3) it allows unhindered access for small molecules and ligands to the proteins, so that interactions and conformational changes when exposed to those small molecules and ligands can be observed.

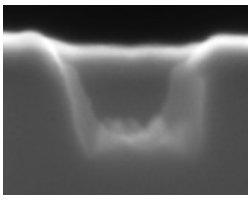

Figure 4.1: SEM image of nanowell. Image taken by Bita Malekian.

Such a device, and its trapping mechanism, is illustrated in Figure 4.2. It is based on plasmonic nanopore arrays with small nanocavities previously made by Malekian et al. (see Figure 4.1)[60]. These structures consist of a silica substrate onto which a 30 nm gold film has been deposited. Using colloidal lithography, the gold is not deposited on the substrate on the sites the colloids are adsorbed, and removing the colloids after the gold deposition leaves a small hole in the gold film; which will become the nanopore. Etching the silica substrate generates the nanochamber, and the nanopore in the gold film allows us to chemically modify the entrance.

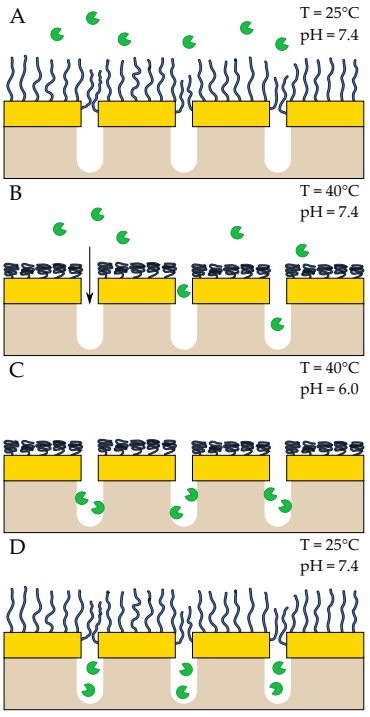

Figure 4.2: Illustration of the thermo-responsive trapping and gating of the nanochamber. (A) At low temperatures the polymer brushes are extended and prevent proteins access to the nanochamber. (B) At high temperatures the brush collapses due to self-interactions, which causes the "gates" to open and allows proteins to enter the nanochamber. (C) At low pH the proteins stick to the interior due to attractive interactions with the silica surface. (D) Decreasing the temperature, and afterwards increasing the pH back to physiological conditions, closes the gates and releases the proteins. The proteins are thus effectively captured inside the nanochambers, as they have no way of exiting through the pore. *This illustration is not to scale.*

The selective trapping mechanism is based on the well-known self-interaction of PNIPAM[3] brushes at elevated temperatures[73]; these allow the brush to switch from an extended to a collapsed state, as mentioned in the theoretical introduction. At low temperatures (<30°C), the brush will be extended and fully cover the nanopore opening (Figure 4.2A). This will deny all macromolecules larger than about 1 kDa[74], such as water, ions and small ligands, access to the nanochamber. Once the temperature is increased, and the macromolecular "gates" are open, the proteins are free to diffuse into the nanochamber. In the open state (Figure 4.2B), the distribution of proteins in the nanochambers should equal the concentration of the solution. So, for instance, at a concentration of 1 µmol L^{-1} we would expect, on average, one protein in the one attoliter large chamber. This can be used to capture only a handful, or even individual, proteins in the nanochambers.

However, in order to get high concentrations of proteins — even higher than the solution concentration — the proteins need to "stick" inside the nanochamber, and long enough for the gates to be closed while they are still inside. This can be done by tuning the degree with which the protein interacts with the glass substrate inside the nanochambers. The main source of interaction between (most) globular proteins and silica is generally agreed to be electrostatic interactions[75–80]. These interactions are most easily tuned by changing the solution pH closer to, or away from, the isoelectric point[77, 81]. There are also reports that hydrophobic interactions and hydrogen bond-formations with the outer water

3: Poly(*N*-isopropylacrylamide)

layer of the surface are involved in stabilising the adsorption of bovine serum albumin (BSA) on silica[81], which is the most well-studied globular protein. Interestingly enough, only parts of the protein actually penetrate this water layer, and it is believed that it is the strong (electrostatic) interactions with these parts of the protein that makes the adsorption possible[80, 81][4].

4: The article by Kubiak-Ossowaska et al. goes into detail on the adsorption mechanism of BSA on silica[81].

BSA, which is the protein that was predominantly used to prove the pH controlled trapping mechanism, has been shown to form complete monolayers at pH 6[81]. Therefore, by introducing the protein at a lower pH and an elevated temperature to the nanochambers, they will adsorb on the silica surface in the nanochambers (Figure 4.2C). Once the proteins are adsorbed, increasing the temperature will close the "gates" while ensuring that the protein remains inside the nanochamber. Note, the solution pH is largely unaffected by changes in temperature in acidic conditions[82], so no premature desorption should occur. Finally, by exchanging the solution back into physiological pH should desorb the proteins, due to unfavourable electrostatic interactions, and the protein is effectively trapped in the nanochamber (Figure 4.2D). Of course, the polymer brush being extended again does not only prevent the trapped proteins from leaving the nanochamber, it also prevents new proteins from entering. This enables studies to be performed with two physically separated domains of, say, an enzyme reaction; making studies of ligand exchange or substrate cycling possible.

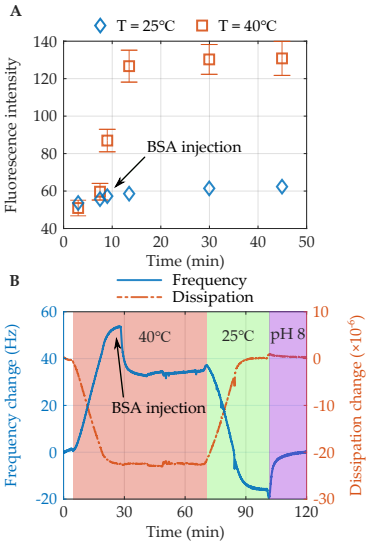

Figure 4.3: Demonstration of the gating and trapping mechanisms of the nanochamber. (A) Fluorescent imaging of a gated nanopore membrane. Fluorescent BSA is only able to diffuse through the pore at 40°C. (B) QCM-D verification of the adsorption and desorption of BSA. Measurements were made by J. Svirelis.

4.3 Conversion of lactose in nanochambers

Previous work done by the main author Justas Svirelis had successfully demonstrated that stable trapping of multiple proteins within the chambers was possible, and that proteins are only able to pass through the nanopore once a certain temperature had been reached and the brushes were collapsed, as shown in Figure 4.3. In Figure 4.3A, fluorescent BSA was introduced to one side of a nanopore membrane — identical to the one in the nanochamber, but without the silica — and only once a threshold temperature was reached did the fluorescence intensity increase on the other side of the membrane. At room temperature the nanopores remained closed to the BSA. This demonstrates the gating mechanism of the device. The multiple protein trapping mechanism was verified with QCM-D, as shown in Figure 4.3B. Here, BSA is introduced to a silica crystal at 40°C and pH 6.0. The adsorption gave an overall reduction in frequency of 20 Hz. The reversibility is demonstrated by lowering the temperature, as per the protocol when working with the nanochambers, and changing the solution pH to 8.0. All BSA was observed to release upon the increase in pH.

Having shown that selective catching and trapping of proteins was successful, the applicability of the devices for bioanalytical studies was investigated with the standard cascade[5] reaction of GAL and GOX to breakdown lactose into d-glucose, and further into H_2O_2 and d-glucono-1,5-lactone (Figure 4.4). QCM-D was used to verify that GOX and GAL were able to bind on silica, as shown in Figure 4.5. The frequency changes for both GOX and GAL were slightly higher than those recorded for BSA (Figure 4.3B), and the kinetics were slower. This is likely due to the greater molecular weight of GOX (160 kDa) and GAL (465 kDa) compared to BSA (66 kDa). As both GOX and GAL are globular proteins, like BSA, and since their isoelectric points are similar[6] it is expected that they interact similarly with the silica. GOX and GAL were also observed to fully release once exposed upon an increase in pH.

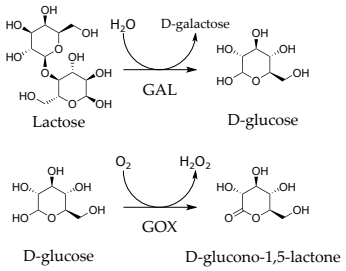

Figure 4.4: Enzymatic hydrolysis of lactose to d-glucose and oxidation of d-glucose to d-glucono-1,5-lactone catalysed by GAL and GOX.

5: An enzymatic cascade reaction is a sequence of successive reactions involving enzymes, where the main product of each preceding reaction is consumed in the next reaction.

6: The isoelectric point of BSA is 4.5-4.8, of GAL 4.6 and of GOX 4.2.

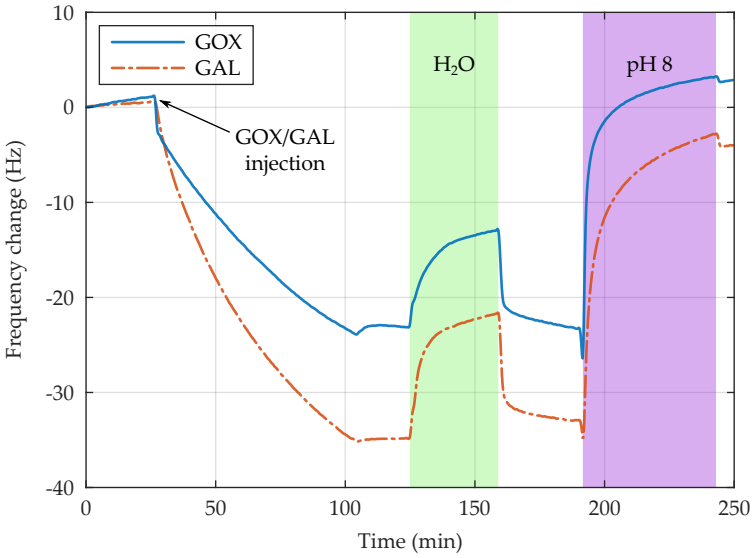

Figure 4.5: Verification of adsorption and desorption of 50 µg/mL GOX (solid) and GAL (dashed) by tuning the solution pH. The running buffer was 150 mM PBS at pH 6.

While the QCM-D data verified that both GOX and GAL were able to adsorb on silica, further verifications that they could bind at the same time was performed with nanochambers modified with PNIPAM brushes. An SEM image of such a chamber, also referred to as a "nanowell", is shown in Figure 4.1. The chambers were loaded by heating a solution at pH 6.0 containing 50 µg/mL GOX and 50 µg/mL GAL to 40°C and exposing the nanochambers to the solution for 60 minutes. The solution was then allowed to cool down, sealing the adsorbed enzymes inside the nanochambers. Native GOX and GAL that had been conjugated with two separate fluorescent dyes — GAL with cyanine-3, which is excited at 511 nm and emits at 569 nm (yellow), and GOX with fluorescein, which is excited at 498 nm and emits at 517 nm (green) — was used for the verification. As can be seen in Figure 4.6, the nanochambers gave signal for both GOX and GAL; indicating that they could

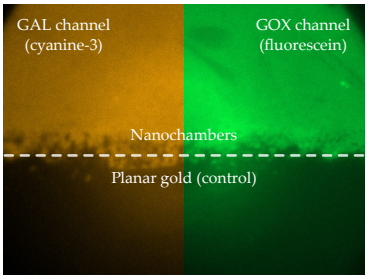

Figure 4.6: Dual-channel imaging of GAL and GOX labelled with fluorescent dyes (cyanine-3 and fluorescein respectively) and trapped together in PNIPAM-gated nanochambers.

be trapped together. While the exact surface coverage — and by extension the relative concentrations once desorbed — of the two enzymes were not investigated further, the high achievable overall concentrations inside the nanochambers should ensure that there is enough of each type of enzyme in each nanochamber[7].

7: We estimate that the nanochambers are able to capture close to 600 individual BSA proteins, so it is not unlikely that each nanochamber contains close to, or even more than, a hundred of each enzyme type.

The activity of the enzymes was investigated with the H_2O_2 sensitive fluorescent probe Amplex red (AR). AR can react with H_2O_2 to create resorufin, which is a fluorescent molecule that is excited at 571 nm and emits at 584 nm (yellow), according to the reaction in Figure 4.7A. This reaction is catalysed by HRP. After loading native GOX and GAL in a similar fashion to the verification experiment, the fluorescent intensity of resorufin was recorded after the injection of a solution consisting of 30 μM AR, 0.1 U/ml HRP and 150 μM lactose. A representative time trace is shown in Figure 4.7B, as well as a control performed without the added lactose.

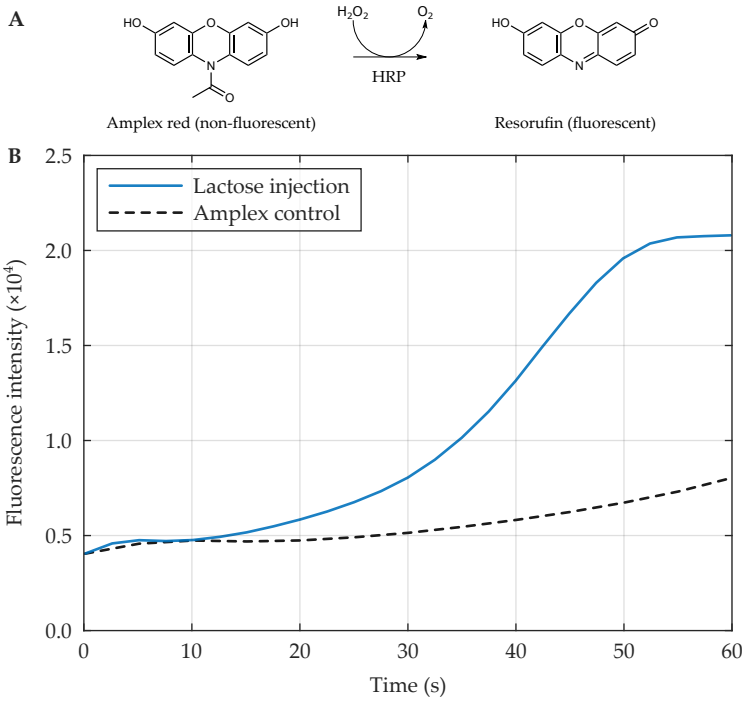

Figure 4.7: Fluorescent detection of the enzymatic cascade reaction in the nanochambers. (A) Reaction of AR with H_2O_2 catalysed by HRP, which generates the fluorescent molecule resorufin. (B) Fluorescence intensity increase from nanochambers with trapped native (unlabeled) GAL and GOX upon introducing lactose, HRP and AR (zero seconds). The control intensity trace had no lactose included, only HRP and AR.

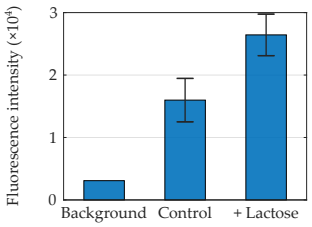

Figure 4.8: Fluorescence intensities after exposing nanochambers with GOX and GAL to 30 μM lactose for 15 minutes (and a control sample).

As can be seen, a considerable amount of resorufin is generated when the lactose is added compared to the control; verifying that the enzymes are active and that reactants (lactose) are able to enter the nanochamber and that the products (H_2O_2) are able to leave. As AR is known to be able to generate resorufin even in the absence of HRP and H_2O_2, a control must always be performed. This is believed to be due to photo-oxidation, from ambient light[83] or even from strong excitation light[84], initiated by trace amounts of resorufin in the sample and further catalysed in the presence of HRP. However, even after 15 minutes, a sample with equimolar lactose to AR still generated a significantly higher fluorescent output, as shown in Figure 4.8; again, demonstrating that H_2O_2

is generated. While the photo-oxidation of AR is troublesome for continuous measurements, such as those performed here where the kinetics were deemed important, this effect would be reduced if the sample was incubated without exposure to light and measured after a set amount of time[8]. Despite the expected high background, the faster recorded kinetics and the higher fluorescent output even after continuous exposure to excitation light for 15 minutes clearly shows that cascade reactions can be successfully run in the nanochambers and that the polymer brush solves the well-known problem of achieving continuous exchange of reactants and products to and from confined enzymes and proteins[85].

8: This is how AR assays are usually used in quantitative studies, and for single measurements no increase in fluorescence is expected[83].

As the device enables binding of high amounts of proteins without immobilization scaffolds or surface adsorption it also allows studying enzymes and proteins in their unmodified native state. Additionally, the high achievable concentrations in the small nanochambers also enables studies on catalytic enhancement effects due to proximity or substrate channelling where intermediary products of cascade reactions are directly transferred from one enzyme to the next, without complete mixing with the bulk phase[86].

4.4 Cofactor cycling of NAD⁺/NADH

Further verification that the nanochambers could be used for biocatalytic applications, where the substrates act as biocatalytic surfaces that perform a certain reaction, was demonstrated with the transport and cycling of the redox cofactor nicotinamide (NADH) and its oxidised equivalent (NAD^+) in and out of the nanochamber. The enzyme alcohol dehydrogenase (ADH) and its oxidation of ethanol to acetaldehyde was used to drive the reduction of NAD^+ to NADH inside the nanochambers. Outside the nanochambers, in the solution phase, the cofactor was cycled back from NAD^+ to the reduced state. The cofactor cycling was driven by the oxidation of d-glucose to d-glucono-1,5-lactone by GOX, which generates H_2O_2, which in turn can reduce NAD^+ to NADH when coupled to the HRP-H_2O_2 cycle as a redox mediator[87]. The overall reaction scheme is shown in Figure 4.9. This is a similar to a cascade cycling system previously described by Lv et al.[88], where ADH and GOX were encapsulated inside peroxidase-like colloids.

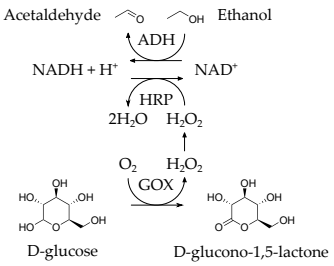

Figure 4.9: Cofactor cyclic reaction of NADH to NAD^+, and then back to NADH, driven by the enzymatic oxidation of ethanol to acetaldehyde by ADH and the oxidation of d-glucose to d-glucono-1,5-lactone by GOX.

ADH was adsorbed within the nanochambers using silica modified with aminopropylsilatrane (APS), according to a previous protocol published by Andersson et al.[89], as this allowed the enzyme to retain its structure upon binding to the surface. The APS here is a "soft coating" compared to the silica to prevent denaturation of the enzyme. The adsorption of ADH on APS-modified silica was verified with QCM-D, as shown in Figure 4.10. The frequency change

was comparable to what was seen for GOX (Figure 4.5), which is expected as the molecular weights of the two are comparable; with ADH at ~150 kDa and GOX at 160 kDa. Rinsing with PBS buffer at pH 7.0, marked by the arrow at ~65 minutes, lead to a steady increase in frequency. This indicates that the enzymes are able to release slowly from the surface after adsorption, and that not all enzymes are attached to the walls during the cofactor cycling

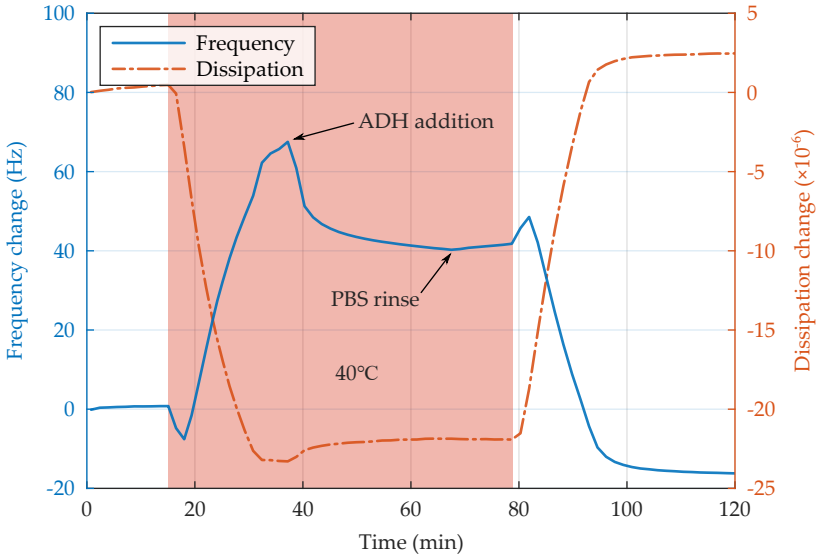

Figure 4.10: Verification with QCM-D of adsorption of 100 µg/mL ADH on APS-modified silica. The running buffer was 150 mM PBS at pH 7.0.

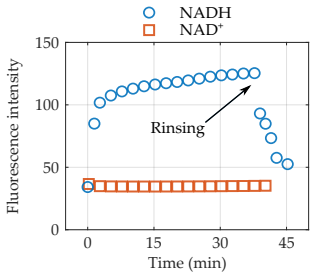

Figure 4.11: Fluorescent verification of the transport of NADH through PNIPAM-modified pores. Measurement by J. Andersson.

NADH is known to absorb in the UV-A region of light[90], with a characteristic peak at ~340 nm. Meanwhile, NAD^+ does not absorb in the same region; allowing us to track changes in absorbance at 340 nm to monitor the reduction of NAD^+ to NADH in real-time. NADH is also known to fluoresce with emission centred around 460 nm when excited at 340 nm[91], which is not the case for NAD^+. Therefore, fluorescence imaging (similar to the one in Figure 4.3B) was used to verify that NADH is able to diffuse through a PNIPAM-gated nanopore membrane (Figure 4.11). NADH and NAD^+, in separate measurements, were introduced to one side of the membrane and the fluorescence was measured on the other side by excitation with a 375 nm LED diode. This is still within the wide absorbance region of NADH. After the injection, the intensity trace clearly shows that NADH is able to pass through the nanopore membrane and emerge on the other side. Upon rinsing, the signal is reduced as NADH diffuses back through the membrane again. Injecting NAD^+ did not generate any fluorescence.

Having shown that transport of NADH through nanopore membranes was possible[9], the cofactor generation and cycling was monitored in-situ with an optical flow setup which allowed for continuous absorbance readout over the nanochambers. Measuring "through" the nanochambers allows us to monitor the generation of

9: This also means that the diffusion of the cofactor and its oxidised state in and out of the nanochambers is possible despite the brushes.

NADH from the reaction with ADH inside, as well as the oxidation back to NAD^+ in the solution above from the reaction with GOX.

With only ADH in the nanochambers, an injection of ethanol gave a positive readout on the absorbance in the UV-A region (Figure 4.12). The absorbance at 340 nm was monitored over time, and a representative time trace is shown in Figure 4.13 (solid line). Over time, the absorbance increased linearly, which confirmed that the ADH remained active inside the nanochambers and that the NAD^+ cofactor is able to diffuse into the nanochamber, undergo the enzymatic reduction to NADH, and then leave the nanochamber. If NADH was to "stick" inside the nanochamber, or if NAD^+ was unable to enter it, the absorbance change would be negligible.

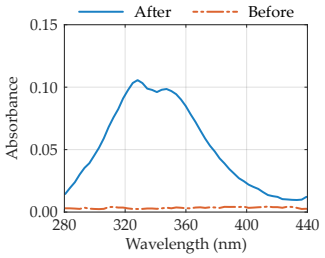

Figure 4.12: Absorbance spectra before and after addition of ethanol (3 hours) to nanochambers containing trapped ADH.

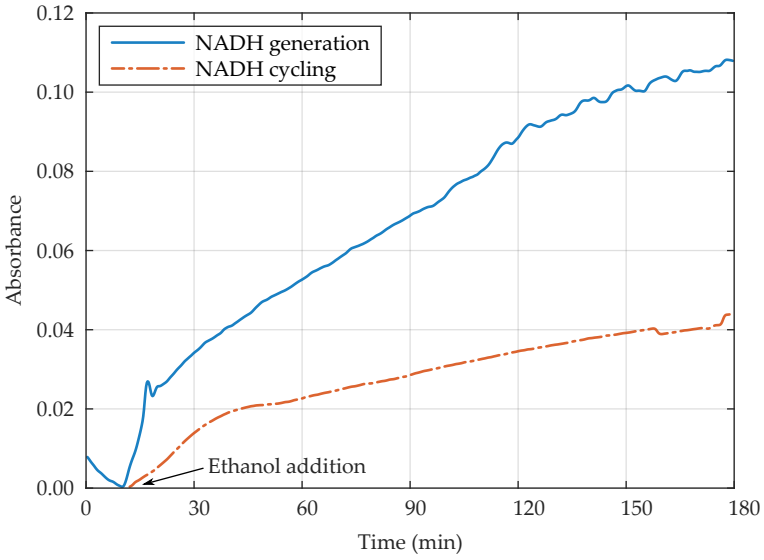

Figure 4.13: NADH cofactor generation (solid) and cycling (dotted) with ADH trapped in nanochambers and with and without GOX, HRP and d-glucose in the solution, in addition to the injected ethanol. The running buffer was 150 mM HEPES pH 7.5.

Introducing GOX, HRP and d-glucose to the solution above the nanochambers led to a reduction in the rate of absorbance increase (dashed). Any generated NADH that leaves the nanochamber is quickly intercepted and reacts with H_2O_2 and HRP to be oxidised back into NAD^+. This NAD^+ is then free to diffuse back into the nanochamber, thus closing the cycle. However, only the generated NADH that leaves the nanochambers can be oxidised since the GOX and HRP are excluded from the nanochambers, which means that a slight increase in absorbance is always expected. Also, all NADH may not react at once in the solution. Nevertheless, the reduction in absorbance increase for the cofactor cycling system demonstrates again that continuous exchange of reactants and products to and from the nanochambers is possible, and that the enzymes maintain their enzymatic activity on the scale of at least several hours once trapped inside the nanochambers.

Enzymatic Polymer Brush Interfaces for Electrochemical Sensing in Biofluids

5

This chapter summarises the second paper presented in this licentiate thesis, "Enzymatic Polymer Brush Interfaces for Electrochemical Sensing in Biofluids". It is currently available as a preprint[4].

5.1 Scientific context

Electrochemical sensors are widely used for selective and sensitive detection of biological markers[92, 93]. This is because of their ability to continuously monitor electron transfer events, making it possible to both detect the presence of electroactive species in the solution as well as quantification of the amount of species at the electrode surface at biologically relevant distances and time scales. These features are relevant for the development of new diagnostic sensors for neural disorders, as they enable the direct monitoring of relevant biomarkers connected to those conditions. Chronoamperometric measurements offer detection of neurotransmitter biomarkers for neurological pathologies, with sub-millisecond temporal resolution[92, 94, 95] and spatial resolution down to single micrometres[96]. This has enabled real-time detection of neurotransmitter release in individual neurons at sub-millisecond resolutions[94, 97, 98], as well as detection of the release of as little as a few thousand molecules[94, 98].

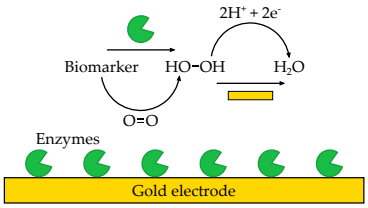

Figure 5.1: Example and working principle of enzymatic biosensing.

However, while some biomarkers, such as dopamine or serotonin, can be directly monitored using electrochemistry, most biological markers are not electroactive; and can thus not be electrochemically detected. This is the case for the two neurotransmitters that are of interest in this study; glutamate and acetylcholine. To overcome this limitation, a biosensor that is chemically selective to each of these biomarkers can be created by attaching enzymes on the surface that convert the non-electroactive biomarker into an electroactive species, commonly hydrogen peroxide (H_2O_2). This has previously enabled detection of both glutamate[99] and acetylcholine[100]. An example of an enzymatic biosensor is shown in Figure 5.1.

However, it is difficult to design a biosensor with an enzymatic interface in which the enzyme can be immobilised in high quantity, while at the same time preserving their activity. In addition, most interfaces cease to function in complex biofluids due to "fouling" of the electrode surface. This is because any matter that binds to the electrode non-specifically will interfere with the ionic electric circuit and hinder electron transfer, thus decreasing the current and selectivity. While polymer brushes are commonly grafted to such surfaces just for the purpose of giving them fouling resistance, the addition of matter from the polymer brush could itself hinder electron transfer and reduce the electrode current[101]. Therefore, a fouling resistant coating must both be able to resist non-specific absorption while allowing unaltered access to the electrode surface for small molecules and substrates to undergo redox reactions. While several potential solutions are possible[1], this study is the first to investigate enzymes conjugated to polymer brushes as dual-function solution to the fouling and immobilisation issues.

1: For example, studies have used hydrogels[102] or conductive porous matrices[101] for enzyme anchoring to achieve the same purpose.

5.2 Enzymatic interface design

In summary, the main considerations that need to be considered for the enzymatic interface is that (1) it has to be able to incorporate enzymes, that (2) it has to give the electrode fouling resistance, that (3) it allows unhindered access for small molecules to the electrode surface, and that (4) the anchoring of the interface to the electrode surface is electrochemically stable.

Such an enzymatic interface is demonstrated in Figure 5.2A. Issues 1 and 2 are solved by the use of PAA[2] brushes, which both offer the innate fouling resistance of the polymer brush, while at the same time containing reactive moieties in the -COOH groups that we are able to use for enzyme conjugation. At physiological pH and salt, electrostatic repulsion between the negatively charged polymers will cause the interface to swell, and the coupled water (in addition to the steric repulsion that the polymers themselves offer) will prevent other biomolecules larger than about 1 kDa[74] from accessing and fouling the electrode surface. As biomarkers generally have lower molecular weights than this threshold[3], there should be little to no issue for the biomarkers to diffuse through the polymer brush, react with the enzymes, and for the generated H_2O_2 to diffuse to and react with the electrode surface.

2: Poly(acrylic acid)

3: For the interest of this study, glucose is 180.16 Da, glutamate is 147.13 Da, and acetylcholine is 146.21 Da.

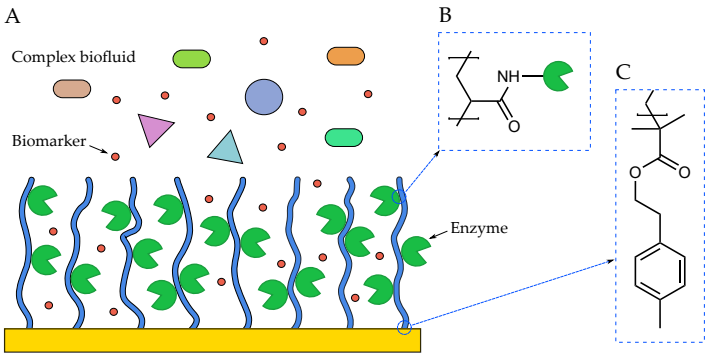

Figure 5.2: Illustration of the interface. (A) The interface incorporates enzymes that can selectively break down biomarkers, while preventing fouling from other biomolecules. (B) Poly(acrylic acid) brushes are functionalized with enzymes by linking -COOH and -NH_2 groups with EDC/NHS chemistry. (C) The brush is securely anchored by electrochemically stable aryl bonds, which also ensures the electrode remains highly accessible for Faradaic reactions.

The immobilisation of enzymes into the polymer brush was done with an EDC/NHS functionalisation (5 mM EDC + 10 mM NHS) of the brush, followed by a covalent amine coupling of the enzyme to the functionalised brush. This results in a permanent (covalent) bond, in the form of an amide, between the enzyme and the brush, as illustrated in Figure 5.2B. The EDC/NHS functionalisation is described in more detail in the methodology. A scheme showing the EDC/NHS functionalisation and the following enzyme coupling reaction is shown in Figure 5.3. It was based on a previous protocol developed by two co-authors in Paper II, G. Ferrand-Drake del Castillo and M. Kyriakidou[103]. Previously, the EDC/NHS functionalisation and the following immobilisation of GOX were both done in 50 mM MES buffer at pH 4.0.sidenote[][*7]Note,

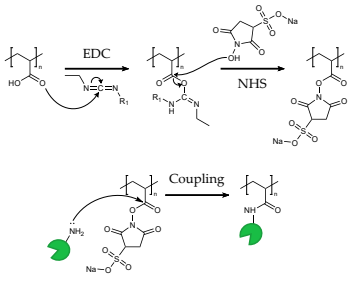

Figure 5.3: Schematic of the initial NHS functionalisation of the PAA brush with the EDC/NHS activation and the enzyme conjugation to the NHS functionalised PAA brush.

Ferrand-Drake del Castillo also used a higher concentration of EDC (40 mM) and NHS (20 mM).. However, the low pH was deemed to be unsuitable for the more sensitive enzymes used for neurotransmitter detection. Therefore, a MES buffer with a higher pH of 5.0, but a lower ionic strength of 10 mM, was used for the immobilisation. Decreasing the ionic strength will increase the pKa, making it possible to protonate the PAA brush at a higher pH[104]. As it is likely strong hydrogen bonding between the enzyme and the PAA brush that is the driving force for interaction[10], and later immobilisation, this solved the issue of protein stability due to low pH while still making the immobilisation feasible[4].

4: In fact, a simulation-based study found that a higher ionic strength lead to more water-protein interactions compared to protein-protein, which in the case of PAA-protein interactions could mean that a lower ionic strength is beneficial[105].

Issue 3 is solved by the use of an polyelectrolyte brush, which are known for their high degree of swelling and water content[106]. As mentioned previously, molecules smaller than about 1 kDa are able to diffuse unhindered through a polymer brush[74], making it a suitable scaffold for the enzymatic interface. Issue 4 is solved by choosing an electrochemically stable anchoring molecule that connects the polymer brush to the electrode surface. Thiolalkanes, which are used for the other polymer brush synthesis in this thesis, are not suitable for electrochemical applications as they are prone to desorb from the surface if exposed to negative voltages[107] and reduce electron transfer rates[108]. An electrochemically stable anchoring layer can be obtained with the diazonium compound[5] attached covalently to the electrode. Monolayers based on diazonium salt precursors are known to be electrochemically stable[109], and have previous electrochemistry applications with polyelectrolyte brushes[61]. Such a diazonium layer is shown in Figure 5.2C.

5: Diazonium compounds are derivatives from aromatic amines that have undergone an elimination reaction to contain the diazonium ([R—N^+≡N]X^-) functional group.

5.3 Surface characterisation

As an initial proof-of-concept, the conjugation chemistry was tested and analysed with the model enzyme glucose oxidase (GOX). SPR was used for quantification of the amount of PAA and bound GOX in the brush via Fresnel modelling in the dry state, as shown in Figure 5.4, as well as to investigate how the hydration of the brush, i.e., ratio of water and polymer, changed after the immobilisation, as shown in Figure 5.5. After the polymerisation, and again after the immobilisation, clear shifts were observed in the SPR spectra. The increase in SPR angle from the polymer coating to after the ex-situ immobilisation of GOX corresponds to an increase of approximately 20 nm, which is the same as having a surface coverage of 2.69 µg/cm^2 GOX using the commonly accepted protein density[6] of 1.35 g/cm^3. As a comparison, the surface density of the polymer itself was 4.32 µg/cm^2, meaning that the brush consists of almost 40% GOX after the immobilisation (on a mass basis). Given that the

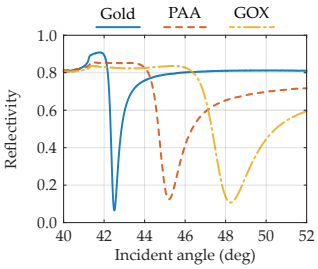

Figure 5.4: SPR spectra measured in air with the 980 nm laser of bare gold (solid), after polymer brush formation (dashed) and after ex-situ GOX immobilisation (dotted).

6: This is a rough estimate. The protein density is most likely a molecular weight-dependent property[110].

dimensions of an individual GOX enzyme is 60×52×77 Å^3[111], the average projected coverage should be 39.1 nm^2 and the maximum surface density of a monolayer should then correspond to 0.68 µg/cm^2. See calculations in the margin[7]. As this is only 25% of the surface density of the average GOX sample, it clearly indicates that the GOX is able to bind in multilayers within the hydrated polymer brush and be able to reach deep within the brush during the conjugation process via so called ternary adsorption.

A densely packed GOX monolayer, where each enzyme uses 39.1 nm^2, contains 2.55×10^{12} enzymes/cm^2, or 4.23 pmol/cm^2. As the molecular weight is 160 000 g/mol, this equals a surface density of 0.68 µg/cm^2.

$$\Gamma_{GOX} = \frac{1}{A_{GOX}}$$

$$\varrho_{GOX} = \Gamma_{GOX}\left(\frac{M_{GOX}}{N_A}\right)$$

This exceptionally high capacity of protein binding has long been believed to be because of electrostatic interactions between the polymer brush and the protein[112]. However, more recent evidence suggests that it is a combination of hydrophobic interactions and hydrogen bonding between the protonated polymer and the protein that is the main driving force between the interactions[104]. In the case with NHS-modified PAA, hydrophobic interactions should be a significant attractive force due to the loss of COOH-units.

7: Reference measurements on gold with a COOH-functionalised anchor layer gave a monolayer coverage of 0.70 ± 0.01 µg/cm^2, which indicates that the GOX packs as tightly as it can or that it favours a more upright distribution on the surface.

The hydration properties of the brush before and after the immobilisation of GOX were investigated using the non-interacting probe method, with 20 mg/ml 35 kDa PEG as the non-interacting probe. The polymer itself showed a great degree of hydration, swelling to almost 10 times its thickness in the dry state, and a high, but reduced, swelling close to 3.5 times compared to the dry state was observed after the enzyme immobilisation[8]. However, when comparing just the water content of the brush, the brush after enzyme immobilisation still consists of over 70% water. The same number before the immobilisation is almost 90%. In fact, even despite the incorporation of enzymes into the brush, it still contains a similar amount of water as neutral polymer brushes, such as PNIPAM[3] and PHEAA[113], when completely swollen.

8: This is likely due to incorporation of charges into the brush leading to more electrostatic self-interactions, which would counteract the same-charge repulsion that gives polyelectrolytes their high swelling ratios, as well as cross-linking where one enzyme binds to more than one chain, which would conformationally limit the swelling of the brush.

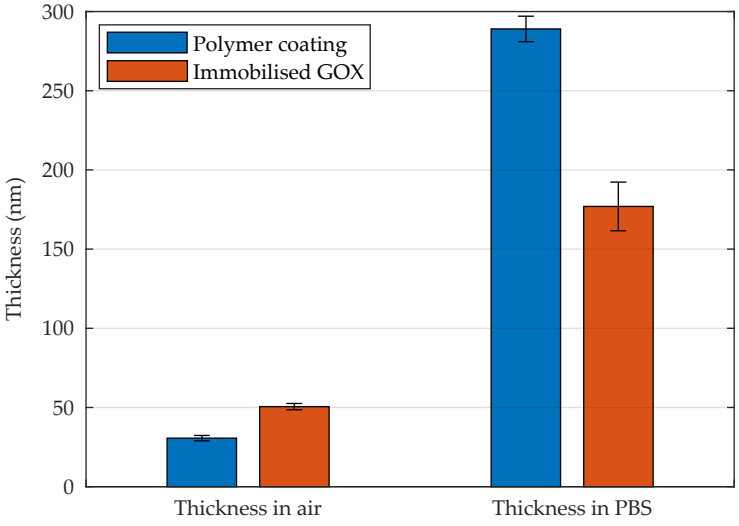

Figure 5.5: Dry thicknesses and exclusion heights calculated from SPR measurements in PBS at pH 7.4, after ATRP and enzyme conjugation. Error bars are from replicates.

The EDC/NHS functionalisation and the following conjugation of GOX was also monitored in real-time with SPR, as shown in Figure 5.6. SPR was measured at three different wavelengths (670 nm, 785 nm and 980 nm) in order to probe the kinetics of the conversion at different depths in the brush. In essence, the longer the wavelength of the light, the deeper into the solution it measures changes in refractive index. Using Equation 3.1[9], described in the theoretical background, we can estimate the decay lengths[10] to 200 nm (at 670 nm), 235 nm (at 785 nm) and 293 nm (at 980 nm). The respective probe depths are about half of these decay lengths. As the brush used in the experiment was almost 300 nm when fully extended, and since the polyelectrolytes are known for decreasing in thickness when protonated[114], the longest wavelength should be sufficient to probe the overall change in mass on the surface whereas the two shorter wavelength lasers should probe changes in the interior of the brush up to their respective limits.

9: Using $\eta_d = 1.33$ as the refractive index of water and $\varepsilon_m = 9.30$ as the dielectric constant of gold.

10: The actual decay lengths are all slightly smaller since the polymer brush and enzymes increase the water's effective refractive index.

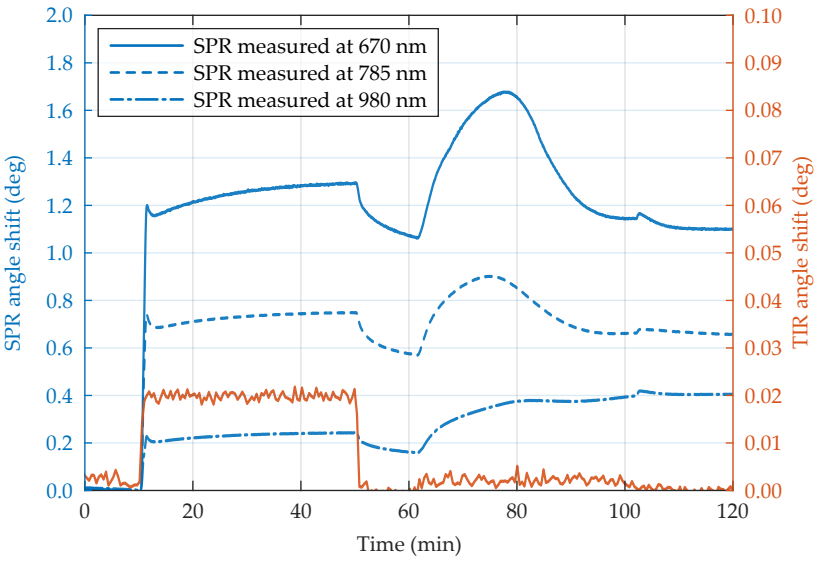

Figure 5.6: In-situ EDC/NHS functionalisation (5 mM EDC + 10 mM NHS) and enzyme conjugation (500 µg/mL) measured with SPR at 670 nm (solid), 785 nm (dashed) and 980 nm (dotted). The running buffer is 10 mM MES pH 5.0. The change in total internal reflection (TIR) angle, which corresponds to the bulk refractive index, is also shown. (A) 40 min EDC/NHS functionalisation followed by rinsing. (B) 40 min GOX immobilisation followed by rinsing. *Note, the TIR shifts are an order of magnitude smaller than the SPR shifts.*

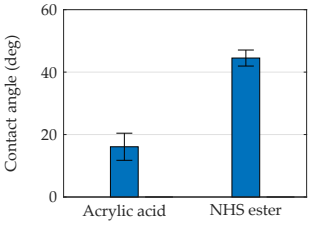

Figure 5.7: Contact angles relative to water before and after EDC/NHS.

During the EDC/NHS functionalisation, marked with "A" in Figure 5.6, all wavelengths showed a similar response, albeit with varying magnitude due to the difference in sensitivity at longer wavelengths. The immediate increase in signal is most likely due to an increase in hydrophobic cohesion within the brush[11], and thus expelling the water, after the conversion of acrylic acid groups to 1-((2-methylbutanoyl)oxy)-2,5-dioxopyrrolidine-3-sulfonate. This can be seen as a significant increase in the contact angle in Figure 5.7, meaning that the surface becomes more hydrophobic after the conversion. A similar increase in hydrophobicity was reported by Schüwer et al. when activating poly(methacrylic acid) brushes with EDC/NHS[115]. After 40 minutes the surface was rinsed with the running buffer, 10 mM MES buffer at pH 5.0, and the slow

11: Using a non-interacting probe to remove the bulk response[49] gave an almost identical angle shift, meaning that the SPR shift should originate from a surface event.

decrease in SPR angle indicated that hydrolysation of the NHS groups was slow, or due to a prolonged liquid exchange.

When GOX was injected to the NHS-activated surface it generated different responses at the three laser wavelengths. Looking at 670 nm, the response is rapid with a distinct "bump" after 15 minutes (at 78 minutes in Figure 5.6), after which the response begins to decrease until the end of the injection 25 minutes later. A similar response is observed at 785 nm, and a clear levelling of the response at 980 nm can be observed after the "bump". This is an indicator that two competing processes are taking place at the same time; one being the immobilisation of GOX, which would increase the SPR angle, and the swelling of the brush[12], which would decrease the SPR angle. As noted before, the 980 nm laser measures changes in the entire brush. Therefore, no more mass, i.e. enzymes, are added to the surface as the response levels out. The "bumps" seen with the 670 and 785 nm lasers can be explained by the swelling of the brush within their evanescent fields. As the polymer brush extends into solution, mass is replaced by water[13], and thus the SPR angle decreases as the total mass within the field decreases.

12: The swelling is likely a result of the introduction of charges into the currently protonated and NHS-modified (neutral) brush; leading to same-charge repulsion.

13: Which cannot be seen by the SPR, as it has the same refractive index as the bulk. Water adds "nothing".

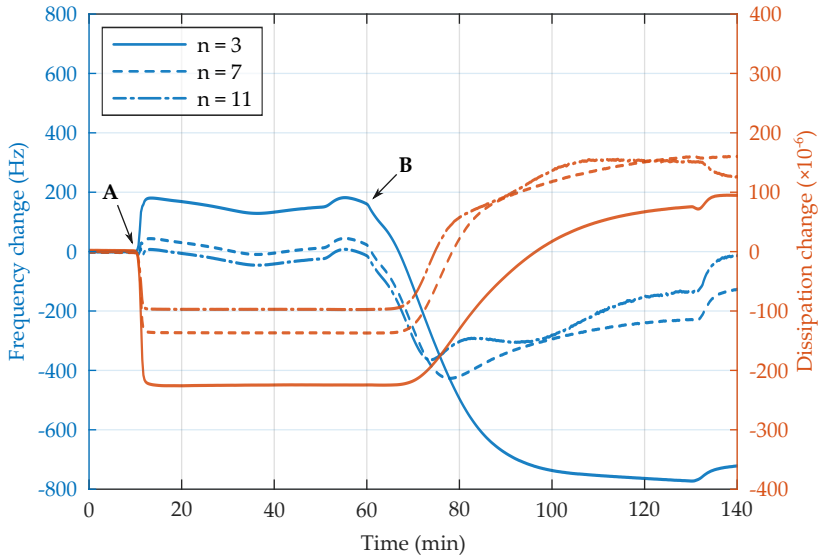

Figure 5.8: In-situ EDC/NHS functionalisation (5 mM EDC + 10 mM NHS) and enzyme conjugation (500 µg/mL) measured with QCM-D at different overtones. The running buffer is 10 mM MES pH 5.0. The change in frequency is shown to the left (in blue) and the change in dissipation is shown to the right (in orange). (A) 40 min EDC/NHS functionalisation followed by rinsing. (B) 70 min GOX immobilisation followed by rinsing.

A complementary technique that can be used to investigate this behaviour is QCM-D. Unlike SPR, QCM-D measures not only the adsorption of mass onto the surface, but also of any coupled water that attaches. Also, similar to the SPR, different overtones can be used to probe at different depths into the solution. Using Equation 3.3[14], we can estimate the penetration depths to 138 nm (at $n = 3$), 90 nm (at $n = 7$) and 72 nm (at $n = 11$)[15]. Real-time monitoring of the EDC/NHS activation and GOX conjugation measured with QCM-D is shown in Figure 5.8 with three overtones, $n = 3$, $n = 7$ and $n = 11$. Similar to the SPR trace, the EDC/NHS activation appears to be almost instantaneous. The decrease in dissipation

14: Using $\eta_m = 8.90 \times 10^{-4}$ Pa s as the viscosity of water and $\rho_m = 997$ kg/m^3 as the density of water.

15: Note that the penetration depths are probably somewhat larger as the parabolic concentration gradient of polymer and enzyme greatly affects the films viscosity-to-density ratio.

confirms that the brush is collapsed after the activation and the lack of an increase during the rinse with MES buffer, after 50 minutes in Figure 5.8, confirms that the hydrolysation is indeed slow.

During the GOX immobilisation, marked with "B" in Figure 5.8, we can see an initial rapid decrease in frequency, with little to no increase in dissipation[16]. After 10 minutes exposure, a "bump",similar to what was seen in the SPR occurs at the two higher overtones as the dissipation begins to increase more rapidly. The large increase in dissipation, even greater than the initial value before the EDC/NHS activation, tells us that the adsorbed film becomes more viscous, i.e. less rigid, than it was in its protonated state.

16: The frequency decrease seen before the dissipation increase is over 150 Hz (at $n = 3$), which also indicates multilayer formation of GOX.

As mentioned before, this is likely due to the additional charges of GOX leading to same-charge repulsion and swelling. The slight increase in frequency in the two higher overtones can be explained by the uptake of water dominating over the uptake of enzymes.

5.4 Electrochemical characterisation

Having successfully fabricated and characterised the polymer coatings and made sure that the enzyme immobilisation functioned, an electrochemical evaluation of the electrodes was done with cyclic voltammetry (CV) and electrochemical impedance spectroscopy (EIS). These two techniques allow us to investigate how the electrodes behaviour in a standard redox reaction changes as the polymerisation is done and after the enzymes are immobilised. We used CV to probe for the diffusive properties of the electrodes, i.e., if the polymer coating and enzyme coatings slowed down or prevented diffusion from the solution to the surface, and we used EIS to probe for any changes in charge transfer resistance, i.e., if the coatings affected the electrodes ability to participate in reactions.

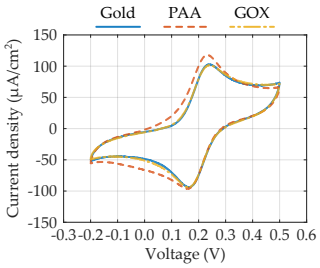

Figure 5.9: CV data (third cycle) of bare gold, after polymer brush formation and after GOX immobilisation measured at 25 mV/s in the presence of 1 mM ferrocenemethanol.

CV was measured at several scan rates, from 10 mV/s up to 360 mV/s, as the peak current of a redox event is correlated to the scan rate and diffusive properties of the redox species, according to the Randles–Ševčík equation described in the methodology (see Equation 3.4). The scans showed very similar responses for the three types of samples, as shown in Figure 5.9, despite the substantial amount of mass added to the electrodes. This suggests that the electrode availability of the redox probe was not significantly altered by the addition of the diazonium salt anchoring layer, the polymer brush, or the enzymes, which is in stark contrast to previous studies done with thiol chemistry[108].

The only notable deviation that was observed was the broadening of the oxidation region +0.15 V to -0.20 V after the polymerisation. We attribute this to the accumulation of the ferrocenemethanol

redox probe within the polymer brush. After the neutral ferrocene turns into the positive ferrocenium ion upon oxidation it can act as a counter ion to the carboxylate groups of the polymer brush and will therefore accumulate close to the surface (see Figure 5.10). Once it undergoes reduction, that is during the anodic sweep from -0.2 V to +0.5 V, it will become neutral again and be allowed to freely diffuse away from the surface. After the enzyme immobilisation, the enzymes themselves would act as counterions to the polymer and therefore this effect would be diminished, which is also what was observed. In fact, the CV of the two samples became nearly indistinguishable. However, this could be the result of two effects; a lowering of the current due to mass accumulation on the surface with a simultaneous local increase in probe concentration.

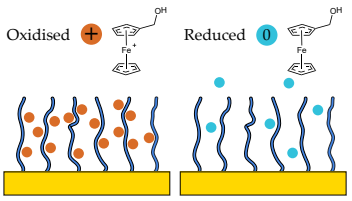

Figure 5.10: Illustration of the accumulation of ferrocenium ions within the polymer brush when oxidised (left) and when reduced (right).

Similar CV curves were recorded at, in total, 8 different scan rates ranging from 10 mV/s up to 360 mV/s. The current maxima during the anodic (-0.2 → +0.5 V) and cathodic (+0.5 → -0.2 V), as seen at +0.25 and +0.15 V respectively at 25 mV/s in Figure 5.9, were plotted in relation to the square root of the scan rate, as shown in Figure 5.11, and a fitting was made using the Randles–Ševčík equation[17]. A clear linear relationship between the square root of the scan rate and the peak current density, as is expected from the Randles–Ševčík equation, can be seen and suggests that the electrochemical processes are diffusion controlled and that the electrode surface is widely available[18]. Using the linear fitting the diffusion constant of ferrocenemethanol can be calculated for the bare electrode to 6.7×10^{-6} cm^2/s, which is comparable to what is reported in literature (7.8×10^{-6} cm^2/s)[116]. Similar values were obtained for the surface after immobilisation of GOX, which strongly suggests that the observed increase in current[19] for the unmodified brush is due to its negative charges as the layer should be closer to neutral after conjugation with GOX.

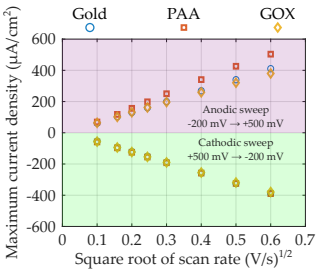

Figure 5.11: Randles-Ševčík plots of peak current values vs scan rate during CV (third cycle) in the presence of 1 mM ferrocenemethanol. The anodic sweeps (top) gave positive currents while the cathodic sweeps (bottom) gave negative currents.

EIS was measured with a DC potential set at the standard redox potential (E_0) of ferrocenemethanol over frequencies ranging from 10^4 to 10^{-1} Hz, with an AC amplitude of 5 mV. Three repeats were run, and the average of these was used for equivalent circuit fitting (see Figure 5.12). The impedance spectra, as shown in Figure 5.13, showed no significant difference between the bare gold, after polymerisation, and after enzyme immobilisation. In fact, a clear lack of a semicircle was observed in all but the sample after enzyme immobilisation. This lack of a semicircle (i.e., a straight line) has previously been reported as characteristic of diffusion controlled electrochemical processes with ohmic connection between the redox probe and the electrode[117, 118], meaning that there is minimal resistance to charge transfer between the two, and is comparable to what is reported in literature for bare gold samples[108, 117, 119]. However, what is different from previous findings is that

17: The Randles–Ševčík equation:

$$i_p = \left(0.4463 nFCA_{\text{eff}}\sqrt{\frac{nFD}{RT}}\right)\sqrt{v}$$

18: Again, the small increase in current during the polymer coating is accredited to ackumulation of ferrocenemethanol in the brush.

19: An increase in the local concentration will linearly increase the current output at the sweep peak.

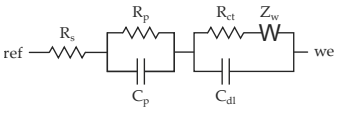

Figure 5.12: Equivalent circuit used in EIS analysis and parameter fitting.

the addition of an initiator monolayer and later polymerisation has no large impact on the impedance of the electrode.

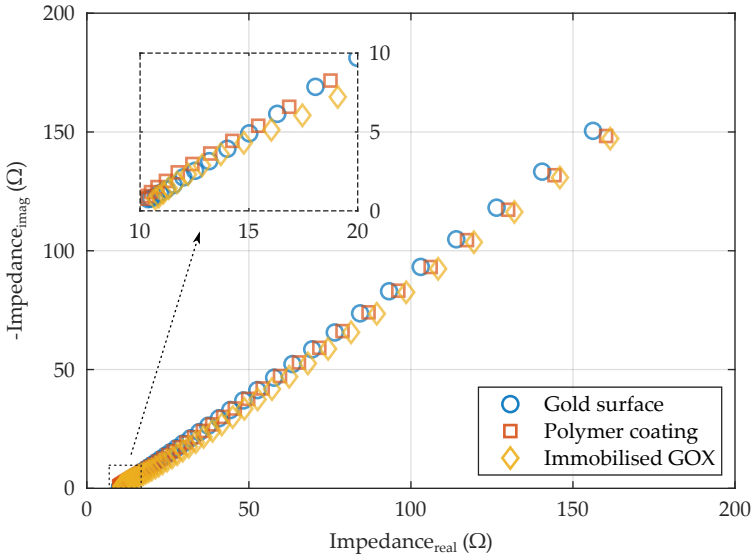

Figure 5.13: EIS spectra in Nyqvist plots measured with 0 DC bias vs the standard redox potential (E_0) of the redox probe (an average of three repeats). The inset shows the higher frequency range up to 10 kHz.

The equivalent circuit shown in Figure 5.12 was used to model the spectrum. It consists of an electrolyte resistance (R_s) in series with a parallel combination of a capacitor (C_p) and resistor (R_p) that corresponds to the polymer and enzyme coatings[20][57], followed by the double-layer capacitance (C_{dl}) in parallel with the charge transfer resistance (R_{ct}) and a mass transfer (Warburg) impedance element (Z_w)[120]. The extracted values of these electrochemical parameters are shown in Table 5.1. On first observation, there is no significant difference in the electrolyte resistance nor the Warburg element, which is as expected as these describe the electrochemical properties of the cell and not the electrode efficiency. After surface functionalisation and enzyme immobilisation, the charge transfer (R_{ct}) increased, but the increase remained extremely low compared to similar systems[108]. This indicates that the surface modifications do not alter the electrode availability towards the redox probe, which is similar to what was observed with CV. It is an "invisible" coating in terms of redox reactivity. The surface capacitance, both in terms of double-layer capacitance (C_{dl}) and polymer brush capacitance (C_p), also increased after the introduction of the brushes and additionally after the enzyme immobilisation. This is likely linked to the increase in electric dipoles and ions on the surface after brush and enzymes are introduced[57]. The polymer brush resistance (R_p) saw a minor increase after the polymer brush and enzymes were introduced, which indicates that the layers had an insignificant impact on the ion migration to the surface.

20: For the bare gold, these two components were not included as they represent the changes in polarizability in the polymer brush coating.

Intuitively, we can compare the length scale of the charge transfer to that of the surface modification, where the redox species and the electrode need to almost "touch" in order for the electrochemical

Surface	Electrochemical parameter in equivalent circuit					
	R_s (Ω)	R_p (Ω)	C_p (μF)	R_{ct} (Ω)	C_{dl} (μF)	Z_w ($mS \times s^{0.5}$)
Bare gold	9.24			0.82	3.08	6.06
Polymer	9.43	0.78	17.1	2.10	50.8	5.99
GOX	10.3	0.99	22.9	3.66	53.1	6.08

Table 5.1: Electrochemical parameters extracted from fitting data of EIS spectra using the equivalent circuit demonstrated in Figure 5.12.

reaction to happen and where the polymer brush is on the scale of hundreds of nanometres when hydrated[21]. So, if the diazonium salt still allows access of ions and the redox species to the electrode, and if the polymer brush do not hinder the diffusion of ions and redox species, the charge transfer should not be significantly affected by the addition of the polymer brush. Similarly, while the enzymes are able to bind in multiple layers within the brush, it is still likely that the majority of the enzymes do not penetrate all the way to the electrode surface. Considering polymer brushes are known for their parabolic monomer distribution[16], enzymes will likely bind in the regions of less density further away from the surface and thus have minimal effect on the redox species ability to access the electrode as long as they do not prevent diffusion through the brush and to the underlying electrode surface.

21: See heights in Figure 5.5.

5.5 Glucose sensing

Having shown that the electrode still remains available to electrochemical reactions after the polymerisation and enzyme immobilisation, the reactivity of the electrode versus glucose and H_2O_2 was investigated. In the enzymatic reaction with GOX and d-glucose, as shown in Figure 5.14, the d-glucose is broken down into d-glucono-1,5-lactone. This process generates H_2O_2 as a side product, which is detectable electrochemically and optically[22]. The reactivity of the electrode with H_2O_2, both from direct injections and as a result of enzymatic breakdown of d-glucose, was investigated with cyclic voltammetry, amperometry and optical spectroscopy. These three techniques give us both qualitative and quantitative information on the overall reactivity of the electrode versus H_2O_2, as well as give us a relative measure of the reactivity of the electrode towards glucose after the enzyme immobilisation. The reason it is relative is because the electrochemical techniques will only measure an unknown fraction of the total amount of generated H_2O_2, as it is based on diffusion of the generated H_2O_2 from the polymer brush to the electrode surface. There is likely to be an equally high, or higher, driving force for the diffusion to occur out into the solution where it cannot react with the electrode.

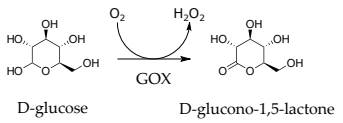

Figure 5.14: Enzymatic oxidation of d-glucose to d-glucono-1,5-lactone catalysed by GOX.

22: A third way to probe the activity is to quantify the electron transfer relative a redox mediator, such as ferrocenemethanol, during the conversion[117]. While this could be more sensitive, we opted for the detection of H_2O_2 as that is the intended application of the biosensor.

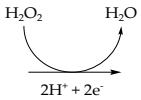

Figure 5.15: Electrochemical reduction of H_2O_2 to H_2O.

CV was measured at 100 mV/s with sample after polymerisation and GOX immobilisation versus PBS, i.e. just the buffering medium, 1 mM d-glucose and 1 mM H_2O_2, as shown in Figure 5.16. The reaction scheme is shown in Figure 5.15. Note, while the existence of H_2O_2 will lead to an enhancement in electrochemical reactivity at certain voltages, there can be other substances in the solution or on the surface that can react as well, for instance oxygen[61], which explains why the signal is not zero in the reference measurement with PBS. Overall, as can be observed in Figure 5.16, the electrode is able to react with H_2O_2, giving quite a large steady-state signal compared to the PBS, and after being exposed to 1 mM d-glucose for 20 minutes, the GOX generated a measurable amount of H_2O_2.

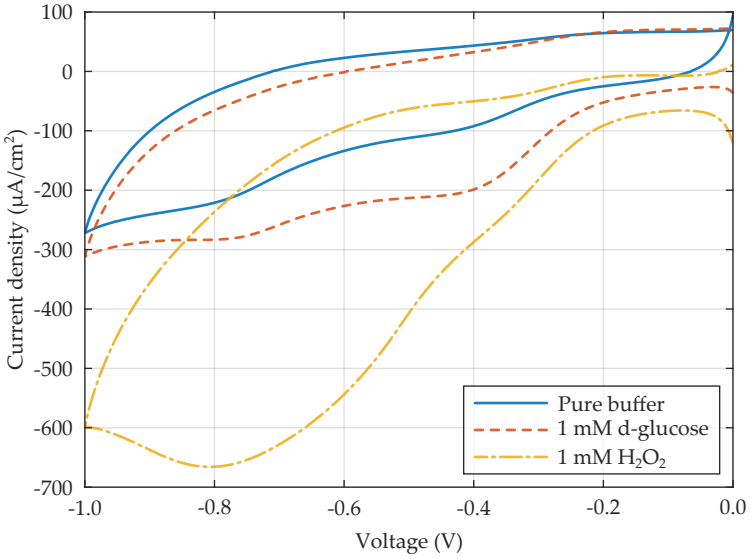

Figure 5.16: Current response from cathodic (+0.0 ⟶ -1.0 V) sweeps (100 mV/s) in PBS buffer, with either 1 mM H_2O_2 or 1 mM d-glucose added.

The reduction of H_2O_2 reached a maximum contrast, relative to the background buffer, at -0.7 V (vs Ag/AgCl). This is slightly more negative than the early reported reduction peak at -0.5 V for clean gold electrodes[121], which suggests that the surface modification has a noticeable impact on the electron transfer reaction[23]. In fact, the presence of organic molecules on the electrode is known to diminish the electrochemical availability due to competitive adsorption[121]. As the electrodes have undergone several treatments prior to their evaluation[24], including polymerisation and surface functionalisation, it is likely that trace chemicals still exist and can affect the electrochemical sensitivity of the surface. Despite this, it is worth noting that the electrode is very much able to detect 1 mM H_2O_2 with a relatively high signal-to-background ratio of 3.60.

Amperometry was used to get comparative electrochemical signals from the d-glucose conversion, as well for investigating the response time of the electrode to burst injections of d-glucose.

23: Due to the sensitivity of the surface coatings to the cleaning protocols used for electrode preparation, often Piranha washing or abrasive polishing, the electrodes cannot be considered completely 'clean'.

24: CV of H_2O_2 done on a fresh gold electrode gave the expected peak at -0.5 V. This indicates the shift is due to the surface modifications.

All amperometry measurements shown were done at the maximum contrast potential of -0.7 V. The obtained signals for two measurements done over 20 minutes with 0.1 mM and 1.0 mM d-glucose done after were integrated to get the overall charge transfer density, and the resulting time plots are shown in Figure 5.17. To avoid any bias from accumulation of H_2O_2 over time, the surface was exposed to a -0.7 V potential prior to the amperometry. Therefore, the charge transfer densities recorded are due to the continuous diffusion and reaction of d-glucose from the solution to the electrode. The slight irregularity where the 10x increase in concentration did not generate a 10x increase in signal is likely due to the well-known inhibition of GOX when exposed to high concentrations of H_2O_2[122]. This would lower the overall reactivity, thus limiting the rate at which the enzyme can produce the H_2O_2.

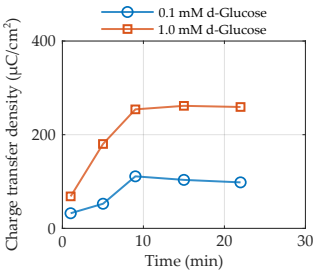

Figure 5.17: Charge transfer density response vs time. Integrated currents (25 s chronoamperometry) performed after different hold times, for two concentrations of d-glucose.

While the enzymes are working as intended inside the polymer brush, an important aspect of biosensors is the response time. That is, how fast after coming in contact with an analyte will the biosensor give a measurable signal. This was investigated with time-resolved chronoamperometry with a resolution of 20 ms, and an example is shown in Figure 5.18. After the injection of d-glucose, a decrease in current was detected almost instantly, reaching a maximum value after 2.4 s and then saturating after approximately one minute. This demonstrates that the electrodes are viable for real-time measurements, albeit with hardware that can measure at higher frequencies.

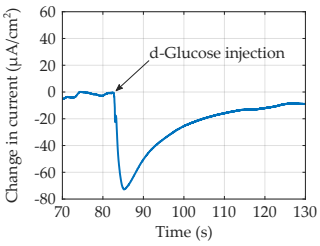

Figure 5.18: Real-time amperometry with an injection of 1 mM d-glucose solution onto the electrode after immobilisation of GOX.

An optical colorimetric assay[25] was used to quantify the amount of glucose that the electrode could generate over time in comparison to the same amount of enzyme in solution. Unlike the electrochemical measurements, which gives primarily a qualitative verification that the reaction works as intended, the optical measurements are not limited by the diffusion of the H_2O_2 to the electrode. Instead, the optical measurements should give a better representation of the actual amount of converted d-glucose. However, the reaction with immobilised enzymes are still likely limited compared to enzymes free in solution as d-glucose has to diffuse from the solution to the electrode surface, compared to GOX free in solution where it can approach from any angle and the enzymes are homogeneously distributed in the solution instead of attached to a surface.

25: This is the FOX assay described in the methodology. It measures the change in absorption at 580 nm.

The absorbance spectra of a sensor with immobilised GOX and of the equivalent amount of GOX free in solution, which was verified from dry measurements done in SPR (similar to Figure 5.4), are shown in Figure 5.20. The sensor showed a measurable amount of converted d-glucose after being exposed for 10 minutes, as did GOX free in solution. However, while it is tempting to compare

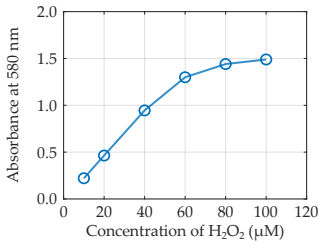

Figure 5.19: Calibration curve at 580 nm of the FOX assay used.

26: This is under the assumption that the calibration is approximately linear between the measured points.

the two absorbance spectra, FOX is known to be linear for only low H_2O_2 concentrations[123], making any conclusions from the spectra itself misleading. Instead, a calibration curve was made with H_2O_2 (Figure 5.19). The assay is linear in the range from 0 to 40 μM H_2O_2, with a slope of 0.02413 μM^{-1}, and in order to measure concentrations above the linear regime the measured absorbance can be directly compared to the calibration curve[26].

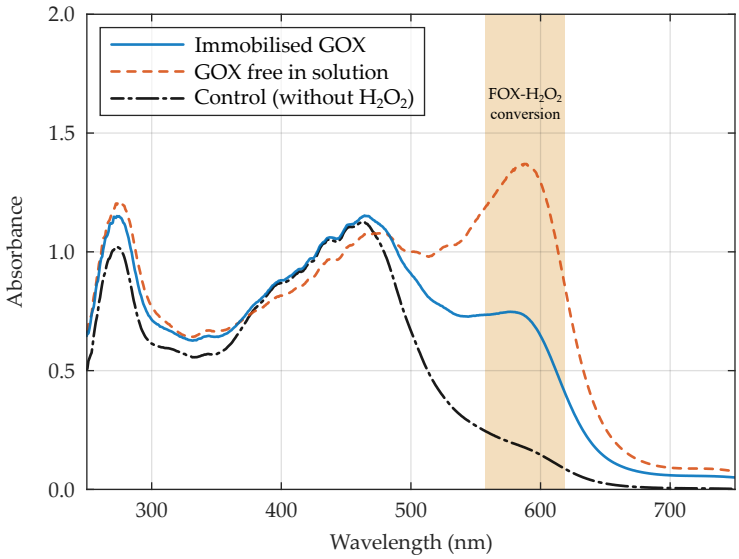

Figure 5.20: Colorimetric verification of H_2O_2 production by immobilised GOX at the sensor surface compared to the response by the same quantity of GOX when free in bulk solution. The absorbance increase at 580 nm is due to H_2O_2.

Using the curve gives a total conversion of 23.6 μM d-glucose from the immobilised GOX and 53.9 μM from GOX in solution, or that the enzyme unit[27] of the immobilised GOX was 1.6 U/mg and 3.7 U/mg for GOX free in solution. This corresponds to a comparative activity of 43.8% on the surface. GOX has previously been reported to retain its full activity upon immobilisation[103, 124], or even showing enhanced activity under certain circumstances, such as in the case of Wang et al. when immobilised onto highly curved surfaces[99]. GOX is known to be very robust[125], and while there are reports that GOX can become deformed when immobilised on solid surfaces[126–128], the "softness" of the polymer brush should prevent enzyme flattening from occurring.

27: The enzyme unit is defined as the amount of the enzyme that catalyzes the conversion of one micromole of substrate per minute.

Therefore it is likely that the lowered activity here compared to measurements in solution is due to mass transport limitations, and due to lack of availability of the innermost enzymes deep in the brush, as d-glucose could be primarily consumed by GOX located in the outer reaches of the brush (see Figure 5.21)[28].

28: This issue would not be prevalent in GOX free in solution, as all GOX have access to the d-glucose.

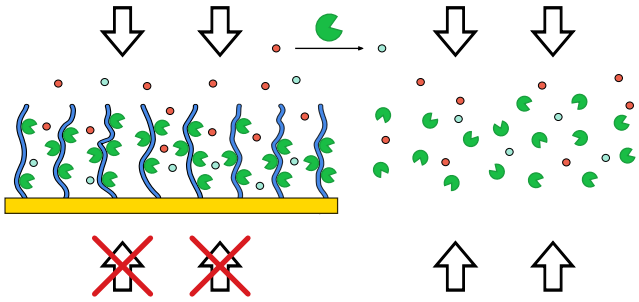

Figure 5.21: Illustration of the mass transport limitation with the sensor compared to a bulk reaction.

5.6 Neurotransmitter sensing

Having shown that the sensor works for enzymatic detection of d-glucose, which again is a common standard enzyme, the versatility of the brush interface was demonstrated with the detection of two neurotransmitters, glutamate and acetylcholine, the latter of which is detected as part of a enzymatic cascade reaction between two different enzymes. These two are important and well-studied biomarkers for neuroscience and neurological disease. In both cases, the enzymes involved generate H_2O_2 by catalysing oxidative reactions. In the former, 1 mole of L-glutamate is converted into 1 mole α-ketoglutarate and 1 mole H_2O_2, catalysed by glutamate oxidase (GluOX) as shown in Figure 5.22. In the latter, 1 mole of acetylcholine is converted into 1 mole of choline and 1 mole of acetic acid, catalysed by acetylcholinesterase (AChE). The 1 mole of choline is then further converted into 1 mole of glycine betaine and 2 moles of H_2O_2, catalysed by choline oxidase (ChOX). Both of these steps are shown in Figure 5.23. Unlike the single enzyme reactions in GOX and GluOX, the AChE/ChOX reactions work as a cascade, and it is therefore important that the two enzymes are close together in order to function optimally. Or, in order for the the electrode to work as efficiently as possible, that the primary conversion of acetylcholine occurs up towards the outer parts of the brush interface, which the molecules will encounter first, and that the subsequent generation of H_2O_2 occurs close to the surface.

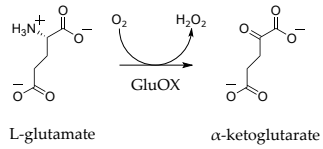

Figure 5.22: Enzymatic oxidation of L-glutamate to α-ketoglutarate catalysed by GluOX.

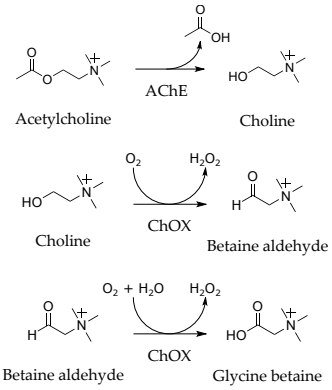

Figure 5.23: Enzymatic oxidation of acetylcholine to glycine betaine catalysed by AChE and ChOX.

Characterisation of the interfaces were done with SPR, CV and EIS with the same conditions as the GOX interfaces. Immobilisation was successful for both the single enzyme and the cascade pair with an average immobilised mass of 1.4-1.5 µg/cm^2. The enzymatic activity of the two interfaces were tested both electrochemically, using the same technique as with GOX. Additionally, the activity of the enzymes were tested in cerebrospinal fluid (CSF), taken from healthy patients at Sahlgrenska University Hospital.

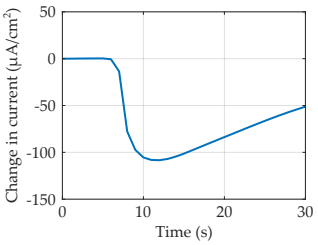

Figure 5.24: Real-time detection of acetylcholine in PBS (1 mM injected over the interface) using the cascade reaction system.

The two interfaces showed selectivity towards acetylcholine and glutamate, respectively, in both the standard PBS buffer solution and in CSF solution, diluted 10x in PBS buffer, as shown in Figure 5.25. While the enzymatic activity was lowered to approximately

50% in 10x diluted CSF compared to in PBS, the interfaces were still able to selectively generate H_2O_2 from the two neurotransmitters to a detectable level. A possible reason for the interference from the biofluid could be that the generated H_2O_2 reacts with antioxidants, such as ascorbic acid, that naturally occurs in CSF[129, 130]. While this will lower the total concentration of H_2O_2 in the solutions that have been exposed for long durations, and thus have had time to generate H_2O_2, it should not have the same impact on "burst" detection, such as the ones shown in Figures 5.18 and 5.24. Ascorbate will consume the initially generated H_2O_2, but once it is used up it will be replaced by pure diffusion. As long as the substrate is supplied to the interface, and generates H_2O_2 that can react with the electrode, faster than this the neurotransmitter should be able to give continuous readouts in CSF as well.

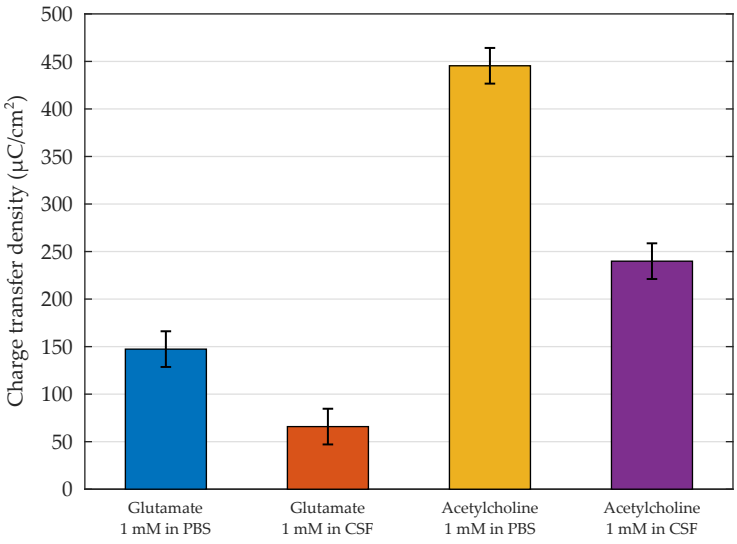

Figure 5.25: Integrated current from chronoamperometry at -0.7 V (for 25 s) for detection of glutamate and acetylcholine using interfaces with GluOX or ChOX + AChE (5:1 molar ratio) respectively. Error bars represent the instrumental variation from repeated measurements.

Unpublished: Nuclear Pore Mimics for Selective Transport

6

This chapter summarises the currently unpublished work done on mimicking the NPCs selective permeability with polymer brushes and polyelectrolyte shuttles. A manuscript is in the works.

Parts of this study is available as a part of mine[131] and a previous student of mines[132] master's theses.

6.1 Scientific context

Ultrathin nanoporous membranes have long been interesting for biofiltering applications, as the high diffusive flux offered by the nanoporous arrays enables a high throughput of analytes under steady-state conditions[133]. However, while the nanopores enable a high diffusive flux of analytes through the membranes, selectivity primarily comes from either size-exclusion, for instance through varying the nanopore geometry[134, 135] or by grafting polymer brushes to reduce the diameter with a soft coating[89], or by charge exclusion[136–138], for instance by applying a potential over the membrane and thus selectively moving negatively charged species to the positively charged electrode, and vice versa. Both of these limit the analyte selectivity and separation possibilities, especially for larger analytes such as proteins, where two species could be distinctly different but have similar enough size and surface charge to not be distinguishable.

A potentially more precise mechanism of separation is with chemical selectivity, where only analytes that "match" the properties of the nanoporous membrane are able to pass through. This type of mechanism is commonly observed in nature, for instance with the bidirectional translocation of biomolecules over the nuclear envelope of eukaryotic cells through the nuclear pore complex[139] (NPC), which is also what inspired this work[1]. Chemical selectivity of nanopores can be achieved by grafting a surface coating over the nanopore that act as a barrier against all macromolecules[2] except for those that fulfil a certain criteria of interaction.

1: A thorough explanation of the function of the NPC can be found in the work of Beck and Hurt[140].

2: Small molecules, such as water and ions, should be able to diffuse unhindered through the nanopore.

Polymer brushes grafted in nanopores have proven to be efficient barriers against proteins while at the same time allowing small molecules (<1 kDa) free access through the nanopore[74]. The well-known antifouling properties of polymer brushes would also prevent clogging of the nanopores, thus extending the lifetime of the membrane. Selective interactions have also been shown to be possible with polymer brushes, where poly(acrylic acid) (PAA) and poly(ethylene glycole) (PEG) interact at low pH through hydrogen bond complexation[141], with the side effect of collapsing the brush. In order for the polymer brush to provide continuous chemical selectivity, the brush needs to remain fully extended.

6.2 Molecular structure of the NPC

The NPC is a large (~120 MDa in humans) complex proteinaceous assembly that serves as a mediator for nuclear transport. It does this by fusing the inner and outer nuclear membrane, forming a pore that allows access between the cytoplasm of the cell and the nucleus. The complex also serves as a stabilising structure for the nuclear pore and it controls the rate of transport of macromolecules in and out of the nucleus using shuttle proteins called karyopherins[140]. An illustration of the NPC is shown in Figure 6.1.

The NPC consists of multiple copies (500-1000 in total) of around 30 distinct protein scaffold groups known as nucleoporins that are arranged into four distinct regions. The core scaffold consists of a subset of outer and inner rings and its associated cytoplasmic and nuclear pore rings (Figure 6.1A), and is in direct contact with the nuclear envelope. The core forms the backbone of the assembly and serves as a structural element, ensuring that the nuclear pore remains stable, and to provide anchoring points for most of the other proteins in the interior parts[142]. The cytoplasmic filaments (Figure 6.1B) and the nuclear basket (Figure 6.1C), which consist of highly flexible protein regions, are located on either side of the assembly and they extend into the cytoplasm and nucleus respectively. These proteins have intrinsically disordered domains, meaning that they lack a fixed or ordered tertiary structure[140], and are involved in the main function of the NPC, where they facilitate the docking of transport receptors and cargo to the assembly[143]. The nuclear basket also serves in a minor role to regulate the curvature of the membrane immediately surrounding it[144]. Lastly, the central channel (Figure 6.1D) contains specific nucleoporins rich in hydrophobic phenylalanine-glycine (FG) repeats and serves as the main mediator for the NPC's selective transport capabilities[139, 142, 145]. The intrinsically disordered nature of the nucleoporins means that the individual proteins located within the central channel are flexible. However, the high concentration of FG repeats generate a high degree of interconnection between nearby proteins through hydrophobic interactions[3]; leading to the formation of an amorphous mesh-like network.

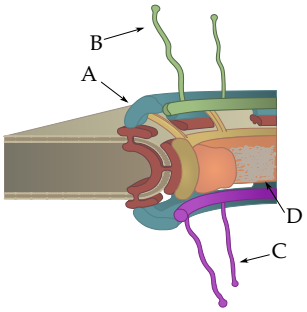

Figure 6.1: Illustration of the NPC with the four distinct regions of interest. (A) The core scaffold. (B) The cytoplasmic filaments. (C) The nuclear basket. (D) The central channel.

3: These interconnections are also believed to have contributions from electrostatic, π-π and π-cation electron interactions, in addition to hydrophobic interactions. Collectively, these are known as *cohesive* interactions, and the role of cohesiveness in the permeability of the NPC is a strongly debated subject. But, the general idea is that only the proteins that can interact with the nucleoporins in the central channel strongly enough to overcome the energetic and entropic barriers of breaking the cohesive interactions are able to pass through the channel[145].

6.3 Mimicking the nuclear transport

When we talk about the nuclear transport mediated by the NPC, the main contributor to both the size exclusion limit, where the channel prevents access to molecules larger than about 40 kDa[146][4], and the selective transport capabilities is the nucleoporins in the central channel and the interactions they offer to certain carrier proteins; the karyopherins mentioned earlier. Therefore, when mimicking the nuclear import and export cycles to make an artificial system for selective transport through a thin membrane, it is the function of the central channel and their interaction with the karyopherins that need to be considered. In summary, the systems needs to (1) have a passive size exclusion where only small molecules, such as water and ions, are able to freely pass through the membrane, it (2) needs to selectively allow one or a few macromolecules access through the membrane via some form of interaction, and (3) that the brush morphology does not change as the shuttle is inserted; that is, even while the shuttles are moving through the selective barrier it should prevent all other macromolecules access.

4: This also means that small molecules, such as water and ions, can move through the tiny "gaps" in the amorphous network unhindered.

Such an NPC mimic is demonstrated in Figure 6.2. Issue 1 (and 2 in part) are solved by the use of PHEAA[5] brushes, which both offer the innate fouling resistance of the polymer brush, while at the same time containing both hydrogen bond donating and accepting moieties[6] (Figure 6.2B). This allows PHEAA to strongly couple water molecules via HB interactions, the likely source of its strong antifouling properties[19]. However, this means that in order for anything to pass through the brush it needs to be small enough to not disturb the HB network, or it needs to be able to interact with the brush enough to overcome the energy barrier that the HB network provides. Issue 2 is also solved by the use of a polymer brush as the diffusion barrier, as the natively intrinsic disorder of hydrated brushes gives the barrier a high degree of flexibility, which is beneficial as it allows the brush to incorporate the additional volume of the shuttle and its macromolecular cargo.

5: Poly(*N*-hydroxyethylacrylamide)

6: Hydrogen bond (HB) donors are moieties that have available hydrogens and HB acceptors have free electron pairs. PHEAA contains both.

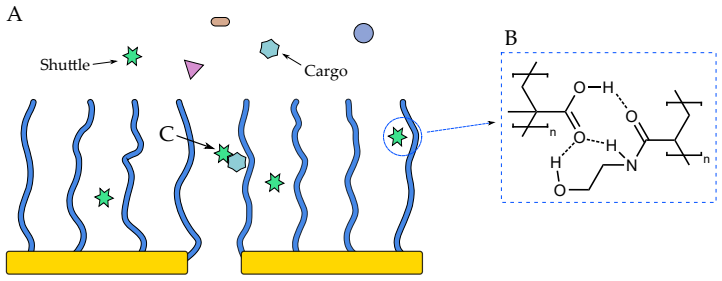

Figure 6.2: Illustration of the NPC mimic. (A) The diffusion barrier is a PHEAA brush that can selectively interact with shuttle molecules, while preventing access for other macromolecules. (B) The shuttle interacts with the brush with hydrogen bonding and other interactions, allowing it to pass through the diffusion barrier. (C) Cargo attached to the shuttle is dragged along through the pore.

Acids, molecules that easily "give up" one or more of their protons, make good candidates as shuttle molecules as they should replace

the water molecules associated to the brush with new thermodynamically favourable hydrogen bonds. However, the large volume of the macromolecular shuttles and their associated cargo, makes it necessary for the shuttle to replaces as many of the HB interactions as possible once inside the brush, to compensate for the increase in free energy from the insertion. Therefore it is necessary to use an acid polymer as the shuttle, of which we chose to use poly(methacrylic acid) (PMAA) for its ability to form strong bonds with neutral polymer brushes[10, 141, 147].

Lastly, the criteria of intact morphology was the reason for choosing PHEAA over the other possible candidates for a brush, as we have found that it strongly interacts with PMAA while at the same time retaining its structural integrity and overall morphology.

Is this a true artificial NPC?

There are two main limitations with this study that prevents it from being a complete artificial reconstruction of the NPC. The study does not implement the "gaps" in the central channel, which refers to the fact that relatively large macromolecules (<40 kDa) are able to pass unhindered through the nuclear pore[146]. While this might be desirable for a biological system, it would be detrimental when designing a selective biofiltration device. However, if such an effect would be desired, it would be possible to increase the overall permeability by, for instance, reducing the grafting density or the thickness of the polymer brush.

The second limitation is the omission of the ranGPT mediated catch-and-release mechanism of the nuclear transport. While cargo transport was investigated, it was attached covalently. A way to improve upon the artificial system would be to include a separable link between the cargo and the shuttle, such as a dithiol bond.

6.4 PHEAA as a diffusion barrier

When designing the diffusion barrier, the thickness of the polymer brush is crucial. It is important that the polymer brush extends out and fills the entirety of the nanopore to fully prevent access to those species that cannot selective interact with the brush. Practically, this means that the average hydrated thickness of the brush must at least match the radius of the nanopore. It being slightly thicker than the radius of the nanopore should not be a concern, as monomer depletion and mass transport limitations during the polymerisation is likely to prevent further growth once the nanopore interior has

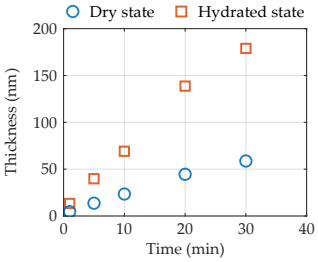

Figure 6.3: Recorded thickness of PHEAA brush in dry and hydrated state with polymerization time.

7: All nanopore samples were polymerised with a separate SPR sensor and the dry and the hydrated thickness was always double-checked.

been saturated. However, we do not want it to be too thick either as it can limit the overall rate of diffusion.

PHEAA was polymerised at different time intervals and the dry and hydrated thicknesses were recorded with SPR, as shown in Figure 6.3. The hydration properties was investigated with the non-interacting probe method, with 20 mg/ml 35 kDa PEG as the non-interacting probe. As can be seen, the polymerisation method offers linear growth of the polymer over all polymerisation times, and the swelling ratio for all the measurements was close to 3.1. In this study, the nanopores used to replicate the nuclear pores were either 80 nm (nanopore arrays) or 120 nm (nanowells). Therefore, in order to completely cover the radius of the pore, a polymerisation time of 10 to 15 minutes is sufficient[7]. In addition to using SPR, the presence of PHEAA on the surface after the polymerisation was verified with FTIR (see Figure A.2 in Appendix A.2).

The ability of the polymer brush to reject larger macromolecules was investigated by injection of BSA (5 mg/ml) and bovine serum (10x diluted) on a surface with a PHEAA brush and a control surface with just gold. The results of those measurements, summarised as fouling density staples, are shown in Figure 6.4. As can be seen, the polymer brush is highly effective at preventing fouling of even highly complex biofluids, such as bovine serum, whereas the gold surfaces experience a high degree of irreversible fouling. Quantitatively, the addition of a PHEAA brush reduced the overall fouling of BSA from 75.5 ng/cm^2 to 0.9 ng/cm^2 and of 10x diluted serum from 325.3 ng/cm^2 to 4.1 ng/cm^2. Both cases showed that PHEAA lowered the fouling by 98.8%. Therefore, PHEAA would serve well as an antifouling barrier for the membrane.

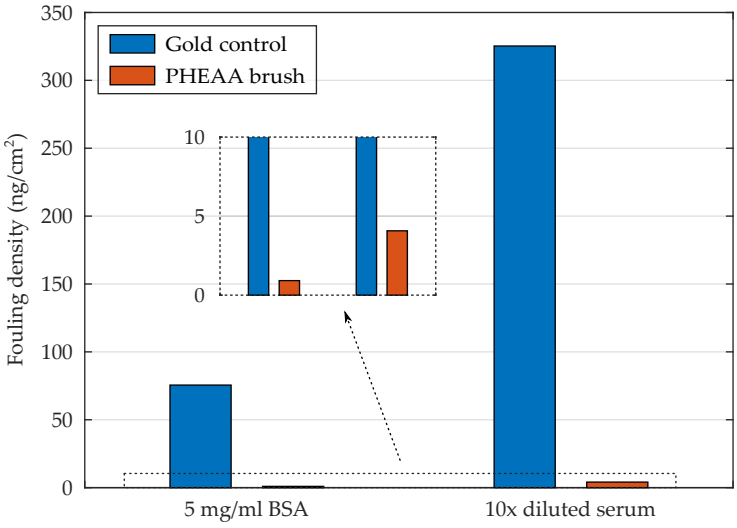

Figure 6.4: Fouling density staples with surface coverage in ng/cm^2 for PHEAA and a gold control.

In addition, the ability of the brush to allow smaller molecules, not

only water and ions, but also larger substrates, to pass through the brush unhindered was investigated by injecting PEG of varying molecular weights and measuring the correlated exclusion height; assuming that PEG acts as a non-interacting probe at all molecular weights (Figure 6.5). A trend of deeper penetration was observed when PEG approached molecular weights below 5 kDa, and there was a clear barrier limit for PEG below 1-2 kDa[8]; terminating at an exclusion height of ~32 nm for the monomer. This is in line with previous findings[74]. The measured exclusion height for the monomer is essentially the same as the dry height (27 nm), which indicates that the PEG has been able to effectively reach the entire volume occupied by water inside the brush.

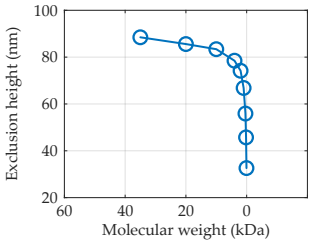

Figure 6.5: Height probing with PEG at decreasing molecular weight to demonstrate the barrier limit.

8: This means that non-interacting molecules are able to pass through the polymer brush once the molecular weight is less than 1-2 kDa.

6.5 Controlling the shuttle permeability

Having verified that PHEAA had the appropriate barrier properties and that it could be polymerised to sufficient thicknesses to fully block the pore, its interactions with a 5 kDa PMAA shuttle at high and low pH was investigated. Being an acidic polymer, the primary driving force for interactions between PMAA and PHEAA should be hydrogen bond formations. This limits the interactions to pH's low enough that PMAA has a sufficient degree of protonation, as this both allows for more hydrogen bonding opportunities[9] and it lowers the overall charge from highly negative to more neutral, which could also have a minor effect on the ability of PMAA to be inserted into the brush. The pH dependence of the interaction between PHEAA and PMAA was characterised with QCM-D, as shown in Figure 6.6 for the fifth acoustic overtone.

9: Importantly, protonation turns PMAA from a pure HB acceptor to both a HB acceptor and donor.

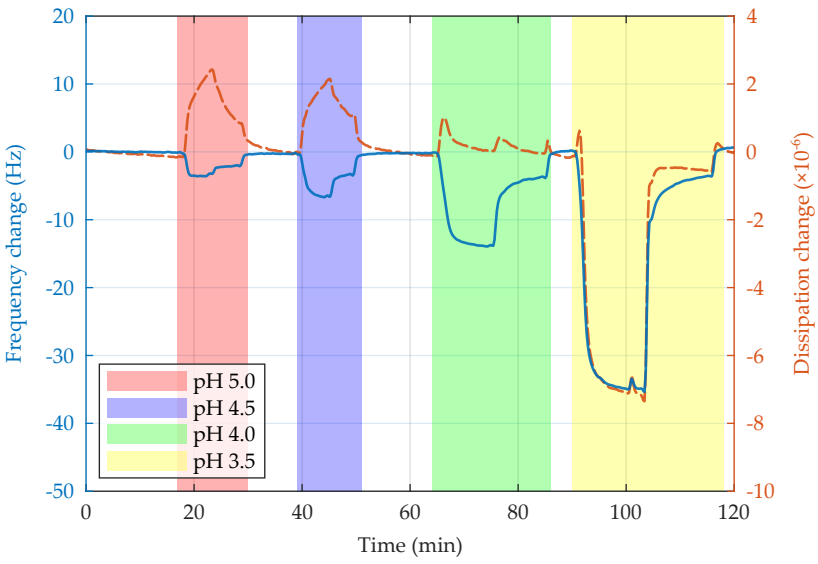

Figure 6.6: pH dependency of the interactions of PHEAA and PMAA from QCM-D. Shown is the change in the frequency (left axis, blue solid) and dissipation (right axis, orange dashed) at the fifth overtone.

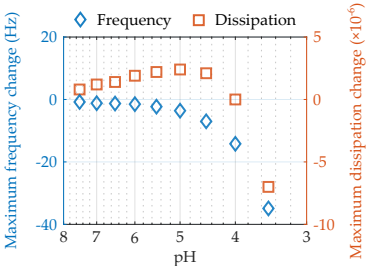

Figure 6.7: Maximum response in the frequency (left axis, solid blue) and dissipation (right axis, orange dashed) at decreasing pH.

10: This could be the polyelectrolyte affecting the bulk properties of the solution close to the surface.

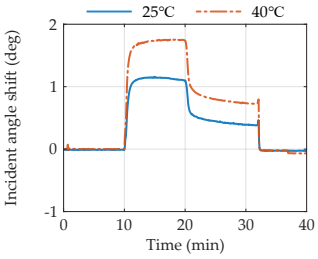

Figure 6.8: Temperature dependence of the interactions of PHEAA and PMAA at pH 4.0. SPR response.

The frequency and dissipation response on PHEAA coated crystals was measured from pH 7.5 to pH 3.5. However, in Figure 6.6 only the measurements close to the transition at pH 4.0 are shown. A clear inversion in the dissipation can be seen at pH 4.0 and below, indicating that crosslinks are beginning to form inside the brush; crosslinks make the brush more rigid, thus lowering the dissipation. The maximum shift in frequency and dissipation for the full pH range is summarised in Figure 6.7. The frequency response steadily decreased after passing pH 5.0, decreasing exponentially faster as the polyelectrolyte became more protonated. Between pH 5.0 and 4.0, which should be the region of the pKa transition for poly(methacrylic acid)[148], the dissipation response also changes from slowly increasing[10], to reaching a maximum value at pH 5.0, and then rapidly decreasing as the pH is lowered further. This tells us that a critical pH value, at which the interactions are strong enough for insertion to occur, is reached once the polyelectrolyte is protonated enough. Further studies of the interactions were done at pH 4.0, as this gave strong interactions and ensured that the solutions remained stable from precipitation.

While it is likely that the primary driving force of the interaction is hydrogen bond formations, there are reports that hydrophobic interactions could contribute to the interaction between the α-methyl group in PMAA and the backbone of hydrophilic polymer brushes, such as PEG, which was studied by Osada et al.[147]. A way to verify the presence of hydrophobic interactions, which is also what they did in the study, is to look at how the interactions change with temperature. Hydrogen bond interactions are expected to decrease as the temperature increases, while hydrophobic interactions are expected to increase[147, 149]. The interaction strength between PHEAA and PMAA, at low pH, was tested at two different temperatures (25°C and 40°C) and this pair of polymer and polyelectrolyte showed a similar increase in intensity at the higher temperature, as shown in Figure 6.8. While the temperature has a minor impact on the pH of the solution[82], it should be small enough to not be responsible for the major increase in signal that was observed. Therefore, the measurement indicates that hydrophobic interactions also exist between PMAA and PHEAA, likely between the α-methyl group in PMAA and the backbone as well as the carbons of the functional side-chain in PHEAA.

6.5.1 Characterising the shuttle-brush interaction

An interesting phenomena that was observed again and again when performing interaction experiments at different pH, see for instance Figures 6.6 and 6.8, was the emergence of a "plateau" of

slow dissociation following a much more rapid dissociation. As the measurements in SPR were all done using the non-interacting probe method to remove the bulk response of the polyelectrolyte, the signal cannot be due to polyelectrolytes close to the surface being washed away. Instead, the measurements indicate that the polyelectrolytes can occupy at least two states within the brush; one "shallow" state which is characterised by weak interactions that are easily broken, and one stronger state which likely is due to polyelectrolytes having undergone tertiary adsorption.

The characteristics of these two adsorption modes were investigated further by injection of PMAA at sequentially increasing concentrations. The Langmuir adsorption model[150], describing the adsorption of a species onto a surface that has a certain number of equivalent binding sites, was used to determine the distribution of the PMAA in these two states under the assumption that the two states are independent of one another. A few of these injections are shown in Figure 6.9. As can be observed, the binding occurs in two modes up until a threshold concentration between 0.2 and 0.8 mM, and that at concentrations between 0.02 mM and 0.1 mM all binding occurs with the slower mode of interaction.

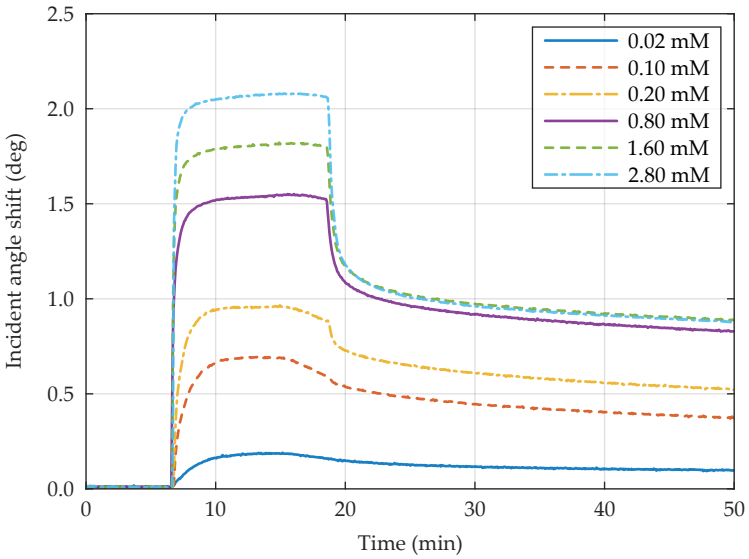

Figure 6.9: Concentration dependence of the interactions of PHEAA and PMAA at pH 4.0. Measured at 25 µL/min with SPR in PBS buffer.

At concentrations below 0.02 mM, only the stronger state appears to be favoured by the shuttle. The slow dissociation of this mode would not be beneficial for transport through a nanopore, as the polyelectrolyte would effectively get "stuck" inside the brush, along with any cargo attached to it. At the higher concentrations above between 0.20 and 0.80 mM the stronger state becomes fully saturated, forcing the transport to occur solely through the weaker mode. However, reaching these concentrations (equivalent to >4 mg/ml) leads to a large loss of polyelectrolytes stuck inside the brush. This limitation can be overcome by either working in the

regime between 0.10 and 0.80 mM, where some polyelectrolyte is stuck to the brush but some also pass through, or by pre-saturating the brush by injecting just the polyelectrolyte before the cargo.

The measured SPR data was also fitted to the Langmuir adsorption model at equilibrium (see equation 6.1), and the resulting fitting as well as the independent modes are shown in Figure 6.10. The model parameters are shown in Table 6.1, where Γ is the saturation limit of the mode and KD is the affinity constant of the mode. "1" represents the slow mode and "2" represents the fast mode.

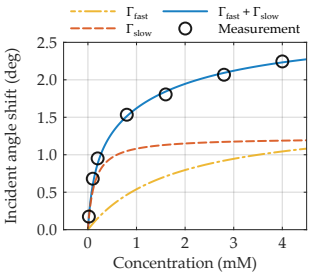

Figure 6.10: Concentration dependence of the maximum SPR response and the fitted adsorption model.

Table 6.1: Model parameters for the Langmuir adsorption model.

Γ_1	KD_1	Γ_2	KD_2
1.229	0.137	1.517	1.812

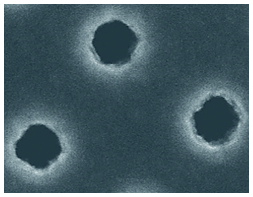

Figure 6.11: SEM image of nanopore. Image taken by Bita Malekian.

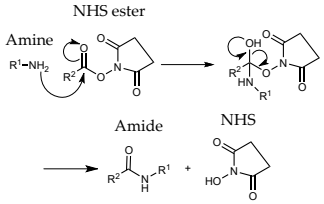

Figure 6.12: Amine-NHS coupling reaction mechanism[152].

$$\Gamma = \frac{\Gamma_{fast} C_0}{KD_{fast} + C_0} + \frac{\Gamma_{slow} C_0}{KD_{slow} + C_0} \tag{6.1}$$

A slow mode of interaction dominates at low concentrations and then saturates at a concentration of 1 mM, while at higher concentrations a fast mode of interactions increases its contribution. While it is possible that a more sophisticated differential model could be developed once more information of the system is known, the simple model gives an almost perfect fitting with the observations. This is similar to what has been previously found in literature. For instance, Emilsson et al. suggested that a two-mode model with an additional sequential transition from a hard to a weak binding mode described the higher order kinetics of a multivalent protein interaction with PEG brushes[13]. Similarly, and related to the transport mechanism of the NPC, Lim et al. found that the interaction between the karyopherins and the nucleoporins had a slower mode at low concentrations that yielded long interaction times and low transport efficiency, while at higher concentrations yielded short interaction times and high transport efficiency[151]; which is exactly what is observed for this system.

6.6 Shuttle-cargo transport of fluorescent dye

Having shown that the interactions between PHEAA and PMAA are viable for allowing transport of the polyelectrolyte, and that ideally transport of cargo through the polymer brush was as well, the shuttle mobility through a nanopore membrane (Figure 6.11) modified with the polymer brush was tested by attaching a fluorescent cargo, either FITC or sulfoCy3, via click-chemistry to a version of PMAA modified to contain an amine end-group (see Figure 6.12 for the amine-NHS coupling reaction mechanism).

Measurements of the transport of sulfoCy3-modified PMAA at pH 4.0 and pH 7.4 showed a high degree of selectivity of transport at the lower pH, as shown in Figure 6.13. Values are normalised[11].

11: The values are normalised relative the maximum (10 minutes) and minimum (0 minutes) values measured over the membrane.

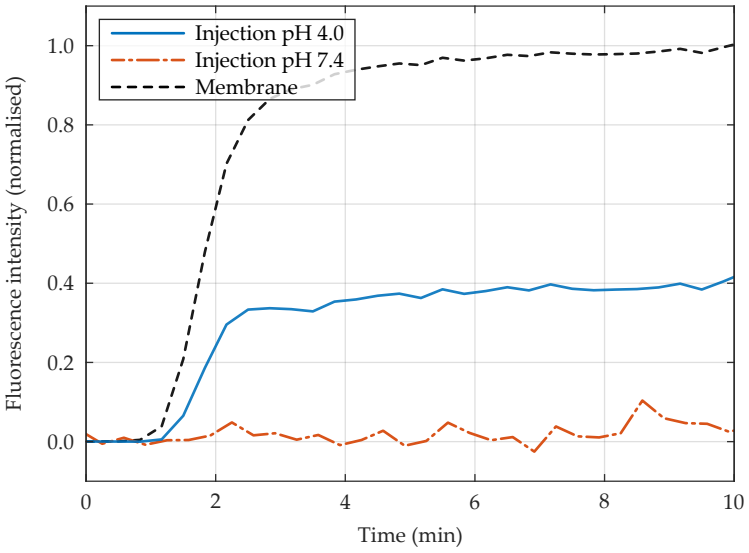

Figure 6.13: Measured fluorescence intensity 40 µm from the outer edge of the nanopore membrane during an injection at pH 4.0 (solid) and 7.4 (dotted). Normalised relative the intensity measured over membrane.

This demonstrates that the interactions between the polyelectrolyte shuttle and the polymer brush do not only allow it the shuttle to enter the brush, but effectively move through it; moving from interaction point to interaction point until it has diffused all the way through the nanopore. The slower diffusion rate after the first minutes could be due to "clogging" of the nanopores by PMAA, as the slow mode of transport is likely to dominate. At longer times, the relative rate of increase is higher outside the membrane than over the membrane (Figure 6.14), which indicates that steady-state transport through the nanopore is occurring; albeit slower than during the initial saturation phase.

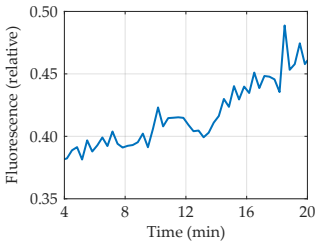

Figure 6.14: Relative fluorescence increase during injection at pH 4.0.

Conclusion and future work 7

This thesis has demonstrated some new developments and applications of polymer brushes for bioanalytical applications for uses in biomolecular trapping, enzymatic biosensing and for selective membrane filtering. Future work will be done on further applications of the new platform for biomolecular trapping, aiming for single-molecule studies of biomolecules, as well as fundamental research on the antifouling properties of brushes; and anything else that might come across my path as I continue my PhD journey.

Paper I has demonstrated the viability of using polymer brushes in the design of novel biomolecular traps, using fabricated nanochambers and thermo-responsive PNIPAM brushes as a "gating" mechanism to selectively capture and confine proteins over long durations. While confined, enzymes retained their activity and were able to catalyse the conversion of lactose into H_2O_2 as well as effectively convert, and cycle, the cofactor nicotinamide using a system where one set of enzymes were trapped inside the nanochambers and one set of enzymes were free in solution above, with the cofactor freely moving to and from the nanochamber.

Paper II has demonstrated the viability of using polymer brushes in the design of novel electrodes for biosensing, using PAA as soft scaffolds for enzyme immobilisation it is possible to create a 3D redox interface where non redox-active biomarkers are converted into redox-active species, which are then detected by the electrode. This was demonstrated to work under physiological conditions and in complex biofluid, showing the robustness of the system.

Bibliography

(1) V. Hlady and J. Buijs, *Current opinion in biotechnology*, 1996, **7**, 72–77 (cit. on p. 1).

(2) M. Hoarau, S. Badieyan and E. N. G. Marsh, *Organic & Biomolecular Chemistry*, 2017, **15**, 9539–9551 (cit. on p. 1).

(3) J. Svirelis, Z. Adali, G. Emilsson, J. Medin, J. Andersson, R. Vattikunta, M. Hulander, J. Järlebark, K. Kolman, O. Olsson et al., *Nature Communications*, 2023, **14**, 5131 (cit. on pp. 1, 3, 23, 37).

(4) J. Medin, M. Kiriakidou, B. Santoso, P. Gupta, G. Ferrand-Drake del Castillo, A.-S. Cans and A. Dahlin, *preprint*, 2024 (cit. on pp. 1, 33).

(5) S. T. Milner, *Science*, 1991, **251**, 905–914 (cit. on p. 3).

(6) G. Fleer, M. C. Stuart, J. M. Scheutjens, T. Cosgrove and B. Vincent, *Polymers at interfaces*, Springer Science & Business Media, 1993 (cit. on pp. 3, 4).

(7) W. J. Brittain and S. Minko, *Journal of Polymer Science Part A: Polymer Chemistry*, 2007, **45**, 3505–3512 (cit. on p. 3).

(8) W.-L. Chen, R. Cordero, H. Tran and C. K. Ober, *Macromolecules*, 2017, **50**, 4089–4113 (cit. on pp. 3, 5–7).

(9) Q. Yu, Y. Zhang, H. Wang, J. Brash and H. Chen, *Acta biomaterialia*, 2011, **7**, 1550–1557 (cit. on p. 3).

(10) G. F.-D. Del Castillo, R. Hailes, Z. Adali-Kaya, T. Robson and A. Dahlin, *Chemical Communications*, 2020, **56**, 5889–5892 (cit. on pp. 3, 36, 53).

(11) J. Yang, H. Chen, S. Xiao, M. Shen, F. Chen, P. Fan, M. Zhong and J. Zheng, *Langmuir*, 2015, **31**, 9125–9133 (cit. on p. 3).

(12) N. K. Mal, M. Fujiwara and Y. Tanaka, *Nature*, 2003, **421**, 350–353 (cit. on p. 3).

(13) G. Emilsson, Y. Sakiyama, B. Malekian, K. Xiong, Z. Adali-Kaya, R. Y. Lim and A. B. Dahlin, *ACS central science*, 2018, **4**, 1007–1014 (cit. on pp. 3, 58).

(14) Y. Jiao, Y. Sun, B. Chang, D. Lu and W. Yang, *Chemistry–A European Journal*, 2013, **19**, 15410–15420 (cit. on p. 3).

(15) Z. Li, M. Tang, S. Liang, M. Zhang, G. M. Biesold, Y. He, S.-M. Hao, W. Choi, Y. Liu, J. Peng et al., *Progress in Polymer Science*, 2021, **116**, 101387 (cit. on p. 3).

(16) S. T. Milner, T. A. Witten and M. E. Cates, *Macromolecules*, 1988, **21**, 2610–2619 (cit. on pp. 5, 11, 16, 43).

(17) J. Zheng, L. Li, S. Chen and S. Jiang, *Langmuir*, 2004, **20**, 8931–8938 (cit. on p. 6).

(18) L. Li, S. Chen, J. Zheng, B. D. Ratner and S. Jiang, *The Journal of Physical Chemistry B*, 2005, **109**, 2934–2941 (cit. on p. 6).

(19) S. Chen, L. Li, C. Zhao and J. Zheng, *Polymer*, 2010, **51**, 5283–5293 (cit. on pp. 6, 52).

(20) S. Jeon, J. Lee, J. Andrade and P. De Gennes, *Journal of colloid and interface science*, 1991, **142**, 149–158 (cit. on p. 6).

(21) E. Ostuni, R. G. Chapman, R. E. Holmlin, S. Takayama and G. M. Whitesides, *Langmuir*, 2001, **17**, 5605–5620 (cit. on p. 6).

(22) D. Nagasawa, T. Azuma, H. Noguchi, K. Uosaki and M. Takai, *The Journal of Physical Chemistry C*, 2015, **119**, 17193–17201 (cit. on p. 6).

(23) S. Chen, J. Zheng, L. Li and S. Jiang, *Journal of the American Chemical Society*, 2005, **127**, 14473–14478 (cit. on p. 6).

(24) T. Otsu, M. Yoshida and T. Tazaki, *Die Makromolekulare Chemie, Rapid Communications*, 1982, **3**, 133–140 (cit. on p. 7).

(25) K. Matyjaszewski and J. Xia, *Chemical reviews*, 2001, **101**, 2921–2990 (cit. on p. 7).

(26) A. Khabibullin, E. Mastan, K. Matyjaszewski and S. Zhu, *Controlled Radical Polymerization at and from Solid Surfaces*, 2016, 29–76 (cit. on pp. 7, 9).

(27) M. K. Georges, R. P. Veregin, P. M. Kazmaier and G. K. Hamer, *Macromolecules*, 1993, **26**, 2987–2988 (cit. on p. 7).

(28) J. Nicolas, Y. Guillaneuf, C. Lefay, D. Bertin, D. Gigmes and B. Charleux, *Progress in Polymer Science*, 2013, **38**, 63–235 (cit. on p. 7).

(29) P. Chmielarz, M. Fantin, S. Park, A. A. Isse, A. Gennaro, A. J. Magenau, A. Sobkowiak and K. Matyjaszewski, *Progress in Polymer Science*, 2017, **69**, 47–78 (cit. on p. 7).

(30) J. McLeary and B. Klumperman, *Soft Matter*, 2006, **2**, 45–53 (cit. on p. 7).

(31) M. Kamigaito, K. Satoh and M. Uchiyama, *Journal of Polymer Science Part A: Polymer Chemistry*, 2019, **57**, 243–254 (cit. on p. 7).

(32) K. Min, H. Gao and K. Matyjaszewski, *Macromolecules*, 2007, **40**, 1789–1791 (cit. on p. 8).

(33) K. Min, H. Gao and K. Matyjaszewski, *Journal of the American Chemical Society*, 2005, **127**, 3825–3830 (cit. on p. 8).

(34) N. V. Tsarevsky and K. Matyjaszewski, *Chemical reviews*, 2007, **107**, 2270–2299 (cit. on p. 8).

(35) W. Jakubowski, K. Min and K. Matyjaszewski, *Macromolecules*, 2006, **39**, 39–45 (cit. on pp. 8, 9).

(36) K. Matyjaszewski and N. V. Tsarevsky, *Journal of the American Chemical Society*, 2014, **136**, 6513–6533 (cit. on pp. 10, 11).

(37) P. Krys and K. Matyjaszewski, *European Polymer Journal*, 2017, **89**, 482–523 (cit. on pp. 10, 11, 20).

(38) S. Thiele, J. Andersson, A. Dahlin and R. L. Hailes, *Langmuir*, 2021, **37**, 3391–3398 (cit. on p. 10).

(39) A. Simakova, S. E. Averick, D. Konkolewicz and K. Matyjaszewski, *Macromolecules*, 2012, **45**, 6371–6379 (cit. on p. 11).

(40) D. Zhou, X. Gao, W.-j. Wang and S. Zhu, *Macromolecules*, 2012, **45**, 1198–1207 (cit. on p. 11).

(41) X. Gao, W. Feng, S. Zhu, H. Sheardown and J. L. Brash, *Macromolecular Reaction Engineering*, 2010, **4**, 235–250 (cit. on p. 11).

(42) M. Manghi, M. Aubouy, C. Gay and C. Ligoure, *The European Physical Journal E*, 2001, **5**, 519–530 (cit. on p. 11).

(43) H. Raether, *Surface plasmons on smooth and rough surfaces and on gratings*, 2006, 4–39 (cit. on p. 13).

(44) J. Homola, *Chemical reviews*, 2008, **108**, 462–493 (cit. on p. 13).

(45) L. S. Jung, C. T. Campbell, T. M. Chinowsky, M. N. Mar and S. S. Yee, *Langmuir*, 1998, **14**, 5636–5648 (cit. on p. 14).

(46) R. L. Schoch and R. Y. Lim, *Langmuir*, 2013, **29**, 4068–4076 (cit. on p. 14).

(47) A. B. Dahlin, *Plasmonic biosensors: an integrated view of refractometric detection*, Ios Press, 2012 (cit. on p. 14).

(48) G. Emilsson, R. L. Schoch, P. Oertle, K. Xiong, R. Y. Lim and A. B. Dahlin, *Applied Surface Science*, 2017, **396**, 384–392 (cit. on p. 14).

(49) J. Svirelis, J. Andersson, A. Stradner and A. Dahlin, *ACS sensors*, 2022, **7**, 1175–1182 (cit. on pp. 14, 38).

(50) D. Johannsmann et al., *Soft and Biological Matter*, 2015, 191–204 (cit. on p. 15).

(51) M. V. Voinova, M. Rodahl, M. Jonson and B. Kasemo, *Physica Scripta*, 1999, **59**, 391 (cit. on p. 15).

(52) M. C. Dixon, *Journal of biomolecular techniques: JBT*, 2008, **19**, 151 (cit. on p. 15).

(53) M. Rodahl and B. Kasemo, *Sensors and Actuators B: Chemical*, 1996, **37**, 111–116 (cit. on p. 15).

(54) K. Xiong, G. Emilsson and A. B. Dahlin, *Analyst*, 2016, **141**, 3803–3810 (cit. on p. 16).

(55) Z.-Y. Jiang, A. C. Woollard and S. P. Wolff, *Lipids*, 1991, **26**, 853–856 (cit. on p. 16).

(56) A. J. Bard, L. R. Faulkner and H. S. White, *Electrochemical methods: fundamentals and applications*, John Wiley & Sons, 2022 (cit. on pp. 17, 18).

(57) J. Anthi, V. Kolivoška, B. Holubová and H. Vaisocherová-Lísalová, *Biomaterials Science*, 2021, **9**, 7379–7391 (cit. on pp. 18, 42).

(58) J. E. B. Randles, *Discussions of the faraday society*, 1947, **1**, 11–19 (cit. on p. 18).

(59) F. C. Anson, *Analytical chemistry*, 1966, **38**, 54–57 (cit. on p. 19).

(60) B. Malekian, K. Xiong, G. Emilsson, J. Andersson, C. Fager, E. Olsson, E. M. Larsson-Langhammer and A. B. Dahlin, *Sensors*, 2017, **17**, 1444 (cit. on pp. 19, 25).

(61) G. F.-D. del Castillo, M. Kyriakidou, Z. Adali, K. Xiong, R. L. Hailes and A. Dahlin, *Angewandte Chemie International Edition*, 2022, **61**, e202115745 (cit. on pp. 20, 36, 44).

(62) J. Jumper, R. Evans, A. Pritzel, T. Green, M. Figurnov, O. Ronneberger, K. Tunyasuvunakool, R. Bates, A. Žídek, A. Potapenko et al., *nature*, 2021, **596**, 583–589 (cit. on p. 24).

(63) L. Cao, B. Coventry, I. Goreshnik, B. Huang, W. Sheffler, J. S. Park, K. M. Jude, I. Marković, R. U. Kadam, K. H. Verschueren et al., *Nature*, 2022, **605**, 551–560 (cit. on p. 24).

(64) P. Fontana, Y. Dong, X. Pi, A. B. Tong, C. W. Hecksel, L. Wang, T.-M. Fu, C. Bustamante and H. Wu, *Science*, 2022, **376**, eabm9326 (cit. on p. 24).

(65) F. Ren, X. Ding, M. Zheng, M. Korzinkin, X. Cai, W. Zhu, A. Mantsyzov, A. Aliper, V. Aladinskiy, Z. Cao et al., *Chemical science*, 2023, **14**, 1443–1452 (cit. on p. 24).

(66) J. Kreitz, M. J. Friedrich, A. Guru, B. Lash, M. Saito, R. K. Macrae and F. Zhang, *Nature*, 2023, **616**, 357–364 (cit. on p. 24).

(67) G. Terashi, X. Wang and D. Kihara, *Acta Crystallographica Section D: Structural Biology*, 2023, **79**, 10–21 (cit. on p. 24).

(68) M. F. Juette, D. S. Terry, M. R. Wasserman, Z. Zhou, R. B. Altman, Q. Zheng and S. C. Blanchard, *Current opinion in chemical biology*, 2014, **20**, 103–111 (cit. on p. 24).

(69) R. Roy, S. Hohng and T. Ha, *Nature methods*, 2008, **5**, 507–516 (cit. on p. 24).

(70) B. Liu, A. Mazouchi and C. C. Gradinaru, *The Journal of Physical Chemistry B*, 2010, **114**, 15191–15198 (cit. on p. 24).

(71) E. Boukobza, A. Sonnenfeld and G. Haran, *The Journal of Physical Chemistry B*, 2001, **105**, 12165–12170 (cit. on p. 24).

(72) J.-Y. Kim, C. Kim and N. K. Lee, *Nature communications*, 2015, **6**, 6992 (cit. on p. 24).

(73) Y. Stetsyshyn, J. Raczkowska, K. Harhay, K. Gajos, Y. Melnyk, P. Dąbczyński, T. Shevtsova and A. Budkowski, *Colloid and Polymer Science*, 2021, **299**, 363–383 (cit. on p. 25).

(74) G. Emilsson, K. Xiong, Y. Sakiyama, B. Malekian, V. A. Gagnér, R. L. Schoch, R. Y. Lim and A. B. Dahlin, *Nanoscale*, 2018, **10**, 4663–4669 (cit. on pp. 25, 35, 36, 50, 55).

(75) H. B. Bull, *Biochimica et biophysica acta*, 1956, **19**, 464–471 (cit. on p. 25).

(76) S. R. Durell, B. R. Brooks and A. Ben-Naim, *The Journal of Physical Chemistry*, 1994, **98**, 2198–2202 (cit. on p. 25).

(77) C. E. Giacomelli and W. Norde, *Journal of Colloid and Interface Science*, 2001, **233**, 234–240 (cit. on p. 25).

(78) K. Rezwan, L. P. Meier and L. J. Gauckler, *Biomaterials*, 2005, **26**, 4351–4357 (cit. on p. 25).

(79) K. Kubiak and P. A. Mulheran, *The Journal of Physical Chemistry B*, 2009, **113**, 12189–12200 (cit. on p. 25).

(80) K. Kubiak-Ossowska and P. A. Mulheran, *Langmuir*, 2010, **26**, 7690–7694 (cit. on pp. 25, 26).

(81) K. Kubiak-Ossowska, K. Tokarczyk, B. Jachimska and P. A. Mulheran, *The Journal of Physical Chemistry B*, 2017, **121**, 3975–3986 (cit. on pp. 25, 26).

(82) J. Ashton and L. Geary, *Tsp*, 2011, **1**, 1–7 (cit. on pp. 26, 56).

(83) B. Zhao, F. A. Summers and R. P. Mason, *Free radical biology and medicine*, 2012, **53**, 1080–1087 (cit. on pp. 28, 29).

(84) H. H. Gorris and D. R. Walt, *Journal of the American Chemical Society*, 2009, **131**, 6277–6282 (cit. on p. 28).

(85) A. Küchler, M. Yoshimoto, S. Luginbühl, F. Mavelli and P. Walde, *Nature nanotechnology*, 2016, **11**, 409–420 (cit. on p. 29).

(86) I. Wheeldon, S. D. Minteer, S. Banta, S. C. Barton, P. Atanassov and M. Sigman, *Nature chemistry*, 2016, **8**, 299–309 (cit. on p. 29).

(87) B. Halliwell and J. d. Rycker, *Photochemistry and Photobiology*, 1978, **28**, 757–762 (cit. on p. 29).

(88) R. Lv, S. Lin, S. Sun, H. He, F. Zheng, D. Tan, B. Ma and M. He, *Chemical Communications*, 2020, **56**, 2723–2726 (cit. on p. 29).

(89) J. Andersson, J. Järlebark, S. Kk, A. Schaefer, R. Hailes, C. Palasingh, B. Santoso, V.-T. Vu, C.-J. Huang, F. Westerlund et al., *ACS Applied Materials & Interfaces*, 2023, **15**, 10228–10239 (cit. on pp. 29, 50).

(90) R. B. McComb, L. W. Bond, R. W. Burnett, R. Keech and G. Bowers Jr, *Clinical chemistry*, 1976, **22**, 141–150 (cit. on p. 30).

(91) J. R. Lakowicz, H. Szmacinski, K. Nowaczyk and M. L. Johnson, *Proceedings of the National Academy of Sciences*, 1992, **89**, 1271–1275 (cit. on p. 30).

(92) Y. Wang, D. Mishra, J. Bergman, J. D. Keighron, K. P. Skibicka and A.-S. Cans, *ACS Chemical Neuroscience*, 2019, **10**, 1744–1752 (cit. on p. 34).

(93) J. Wu, H. Liu, W. Chen, B. Ma and H. Ju, *Nature Reviews Bioengineering*, 2023, **1**, 346–360 (cit. on p. 34).

(94) Y. Wang, H. Fathali, D. Mishra, T. Olsson, J. D. Keighron, K. P. Skibicka and A.-S. Cans, *Journal of the American Chemical Society*, 2019, **141**, 17507–17511 (cit. on p. 34).

(95) M. Ganesana, E. Trikantzopoulos, Y. Maniar, S. T. Lee and B. J. Venton, *Biosensors and Bioelectronics*, 2019, **130**, 103–109 (cit. on p. 34).

(96) I. Hafez, K. Kisler, K. Berberian, G. Dernick, V. Valero, M. G. Yong, H. G. Craighead and M. Lindau, *Proceedings of the National Academy of Sciences*, 2005, **102**, 13879–13884 (cit. on p. 34).

(97) S. E. Hochstetler, M. Puopolo, S. Gustincich, E. Raviola and R. M. Wightman, *Analytical chemistry*, 2000, **72**, 489–496 (cit. on p. 34).

(98) Y. Wang, A. Pradhan, P. Gupta, J. Hanrieder, H. Zetterberg and A.-S. Cans, *Journal of the American Chemical Society*, 2024, **146**, 25902–25906 (cit. on p. 34).

(99) Y. Wang, R. Jonkute, H. Lindmark, J. D. Keighron and A.-S. Cans, *Langmuir*, 2019, **36**, 37–46 (cit. on pp. 34, 46).

(100) J. D. Keighron, S. Åkesson and A.-S. Cans, *Langmuir*, 2014, **30**, 11348–11355 (cit. on p. 34).

(101) J. Sabaté del Río, O. Y. Henry, P. Jolly and D. E. Ingber, *Nature nanotechnology*, 2019, **14**, 1143–1149 (cit. on p. 34).

(102) Y. Yin, H. Zeng, S. Zhang, N. Gao, R. Liu, S. Cheng and M. Zhang, *Analytical Chemistry*, 2023, **95**, 3390–3397 (cit. on p. 34).

(103) G. Ferrand-Drake del Castillo, M. Koenig, M. Müller, K.-J. Eichhorn, M. Stamm, P. Uhlmann and A. Dahlin, *Langmuir*, 2019, **35**, 3479–3489 (cit. on pp. 35, 46).

(104) G. Ferrand-Drake del Castillo, R. L. Hailes and A. Dahlin, *The Journal of Physical Chemistry Letters*, 2020, **11**, 5212–5218 (cit. on pp. 36, 37).

(105) Z. Zhang, Y. Yang, X. Tang, Y. Chen and Y. You, *Food Science and Technology Research*, 2015, **21**, 597–605 (cit. on p. 36).

(106) J. Rühe, M. Ballauff, M. Biesalski, P. Dziezok, F. Gröhn, D. Johannsmann, N. Houbenov, N. Hugenberg, R. Konradi, S. Minko et al., *Polyelectrolytes with defined molecular architecture I*, 2004, 79–150 (cit. on p. 36).

(107) C. A. Widrig, C. Chung and M. D. Porter, *Journal of electroanalytical chemistry and interfacial electrochemistry*, 1991, **310**, 335–359 (cit. on p. 36).

(108) J. Anthi, E. Vaněčková, M. Spasovová, M. Houska, M. Vrabcová, E. Vogelová, B. Holubová, H. Vaisocherová-Lísalová and V. Kolivoška, *Analytica Chimica Acta*, 2023, **1276**, 341640 (cit. on pp. 36, 40–42).

(109) G. Liu, T. Böcking and J. J. Gooding, *Journal of Electroanalytical Chemistry*, 2007, **600**, 335–344 (cit. on p. 36).

(110) H. Fischer, I. Polikarpov and A. F. Craievich, *Protein Science*, 2004, **13**, 2825–2828 (cit. on p. 36).

(111) H. Hecht, H. Kalisz, J. Hendle, R. Schmid and D. Schomburg, *Journal of molecular biology*, 1993, **229**, 153–172 (cit. on p. 37).

(112) J. Dai, Z. Bao, L. Sun, S. U. Hong, G. L. Baker and M. L. Bruening, *Langmuir*, 2006, **22**, 4274–4281 (cit. on p. 37).

(113) J. Medin, B. Santoso†, L. Beckerman†, R. Hailes, R. Vattikunta, J. Andersson, G. F.-D. del Castillo and A. Dahlin, 'Mimicking the NPCs Selective Permeability with Polymer Brushes and Polyelectrolyte Shuttles', In manuscript (cit. on p. 37).

(114) G. Ferrand-Drake del Castillo, G. Emilsson and A. Dahlin, *The Journal of Physical Chemistry C*, 2018, **122**, 27516–27527 (cit. on p. 38).

(115) N. Schüwer and H.-A. Klok, *Langmuir*, 2011, **27**, 4789–4796 (cit. on p. 38).

(116) W. Miao, Z. Ding and A. J. Bard, *The Journal of Physical Chemistry B*, 2002, **106**, 1392–1398 (cit. on p. 41).

(117) S. Zhang, N. Wang, Y. Niu and C. Sun, *Sensors and Actuators B: Chemical*, 2005, **109**, 367–374 (cit. on pp. 41, 43).

(118) D. Premathilake, R. A. Outlaw, S. G. Parler, S. M. Butler and J. R. Miller, *Carbon*, 2017, **111**, 231–237 (cit. on p. 41).

(119) Y. Aceta, Y. R. Leroux and P. Hapiot, *ChemElectroChem*, 2019, **6**, 1704–1710 (cit. on p. 41).

(120) A. C. Lazanas and M. I. Prodromidis, *ACS Measurement Science Au*, 2023, **3**, 162–193 (cit. on p. 42).

(121) M. Gerlache, Z. Senturk, G. Quarin and J.-M. Kauffmann, *Electroanalysis*, 1997, **9**, 1088–1092 (cit. on p. 44).

(122) J. Bao, K. Furumoto, M. Yoshimoto, K. Fukunaga and K. Nakao, *Biochemical engineering journal*, 2003, **13**, 69–72 (cit. on p. 45).

(123) M. del Carmen Pinto, A. Tejeda, A. L. Duque and P. Macías, *Journal of Agricultural and Food Chemistry*, 2007, **55**, 5956–5959 (cit. on p. 46).

(124) G. K. Kouassi, J. Irudayaraj and G. McCarty, *Biomagnetic research and technology*, 2005, **3**, 1–10 (cit. on p. 46).

(125) R. Wilson and A. Turner, *Biosensors and bioelectronics*, 1992, **7**, 165–185 (cit. on p. 46).

(126) A. Szucs, G. D. Hitchens and J. O. Bockris, *Journal of The Electrochemical Society*, 1989, **136**, 3748 (cit. on p. 46).

(127) I. Otsuka, M. Yaoita, S. Nagashima and M. Higano, *Electrochimica acta*, 2005, **50**, 4861–4867 (cit. on p. 46).

(128) B. Kowalewska and K. Jakubow, *Sensors and Actuators B: Chemical*, 2017, **238**, 852–861 (cit. on p. 46).

(129) H. Reiber, M. Ruff and M. Uhr, *Clinica chimica acta*, 1993, **217**, 163–173 (cit. on p. 48).

(130) G.-C. Yen, P.-D. Duh and H.-L. Tsai, *Food chemistry*, 2002, **79**, 307–313 (cit. on p. 48).

(131) J. Medin, MA thesis, Chalmers University of Technology, 2022 (cit. on p. 49).

(132) L. Beckerman, MA thesis, Chalmers University of Technology, 2023 (cit. on p. 49).

(133) P. Stroeve and N. Ileri, *Trends in biotechnology*, 2011, **29**, 259–266 (cit. on p. 50).

(134) R. van Reis and A. Zydney, *Journal of Membrane Science*, 2007, **297**, 16–50 (cit. on p. 50).

(135) H. B. Park, J. Kamcev, L. M. Robeson, M. Elimelech and B. D. Freeman, *Science*, 2017, **356**, eaab0530 (cit. on p. 50).

(136) D. Stein, M. Kruithof and C. Dekker, *Physical Review Letters*, 2004, **93**, 035901 (cit. on p. 50).

(137) A. J. Storm, C. Storm, J. Chen, H. Zandbergen, J.-F. Joanny and C. Dekker, *Nano letters*, 2005, **5**, 1193–1197 (cit. on p. 50).

(138) C. Plesa, S. W. Kowalczyk, R. Zinsmeester, A. Y. Grosberg, Y. Rabin and C. Dekker, *Nano letters*, 2013, **13**, 658–663 (cit. on p. 50).

(139) G. J. Stanley, A. Fassati and B. W. Hoogenboom, Seminars in cell & developmental biology, 2017, vol. 68, pp. 42–51 (cit. on pp. 50, 51).

(140) M. Beck and E. Hurt, *Nature reviews Molecular cell biology*, 2017, **18**, 73–89 (cit. on pp. 50, 51).

(141) J. Andersson, G. Ferrand-Drake del Castillo, P. Bilotto, F. Hook, M. Valtiner and A. Dahlin, *Langmuir*, 2021, **37**, 4943–4952 (cit. on pp. 50, 53).

(142) F. Alber, S. Dokudovskaya, L. M. Veenhoff, W. Zhang, J. Kipper, D. Devos, A. Suprapto, O. Karni-Schmidt, R. Williams, B. T. Chait et al., *Nature*, 2007, **450**, 695–701 (cit. on p. 51).

(143) S. R. Wente and M. P. Rout, *Cold Spring Harbor perspectives in biology*, 2010, **2**, a000562 (cit. on p. 51).

(144) N. Mészáros, J. Cibulka, M. J. Mendiburo, A. Romanauska, M. Schneider and A. Köhler, *Developmental cell*, 2015, **33**, 285–298 (cit. on p. 51).

(145) C. Gu, A. Vovk, T. Zheng, R. D. Coalson and A. Zilman, *Biophysical journal*, 2019, **116**, 1204–1215 (cit. on p. 51).

(146) M. Christie, C.-W. Chang, G. Róna, K. M. Smith, A. G. Stewart, A. A. Takeda, M. R. Fontes, M. Stewart, B. G. Vértessy, J. K. Forwood et al., *Journal of molecular biology*, 2016, **428**, 2060–2090 (cit. on pp. 52, 53).

(147) Y. Osada and M. Sato, *Journal of Polymer Science: Polymer Letters Edition*, 1976, **14**, 129–134 (cit. on pp. 53, 56).

(148) R. Arnold, *Journal of Colloid Science*, 1957, **12**, 549–556 (cit. on p. 56).

(149) J. A. Schellman, *Biophysical Journal*, 1997, **73**, 2960–2964 (cit. on p. 56).

(150) I. Langmuir, *Journal of the American Chemical society*, 1918, **40**, 1361–1403 (cit. on p. 57).

(151) R. Y. Lim, B. Huang and L. E. Kapinos, *Nucleus*, 2015, **6**, 366–372 (cit. on p. 58).

(152) G. T. Hermanson, *Bioconjugate techniques*, Academic press, 2013 (cit. on p. 58).

(153) P. Larkin, *Infrared and Raman spectroscopy: principles and spectral interpretation*, Elsevier, 2017 (cit. on pp. 74–76).

Appendix

Appendix A: FTIR Analysis

A.1 FTIR of PAA

Poly(acrylic acid) has two notable IR regions (Figure A.1), a wide band from 3700 cm^{-1} to 2400 cm^{-1} and a peak at 1730 cm^{-1}.

A wide band from 3700 cm^{-1} to 3100 cm^{-1} is associated with O-H vibrations (blue), and the extension of the band into the range of 3100 cm^{-1} to 2400 cm^{-1} is characteristic of the strong hydrogen bonding of the acidic hydrogens in carboxylic acids. The peak at 1730 cm^{-1} is associated with C=O stretching in the carbonyl group (red) of a carboxylic acid[153].

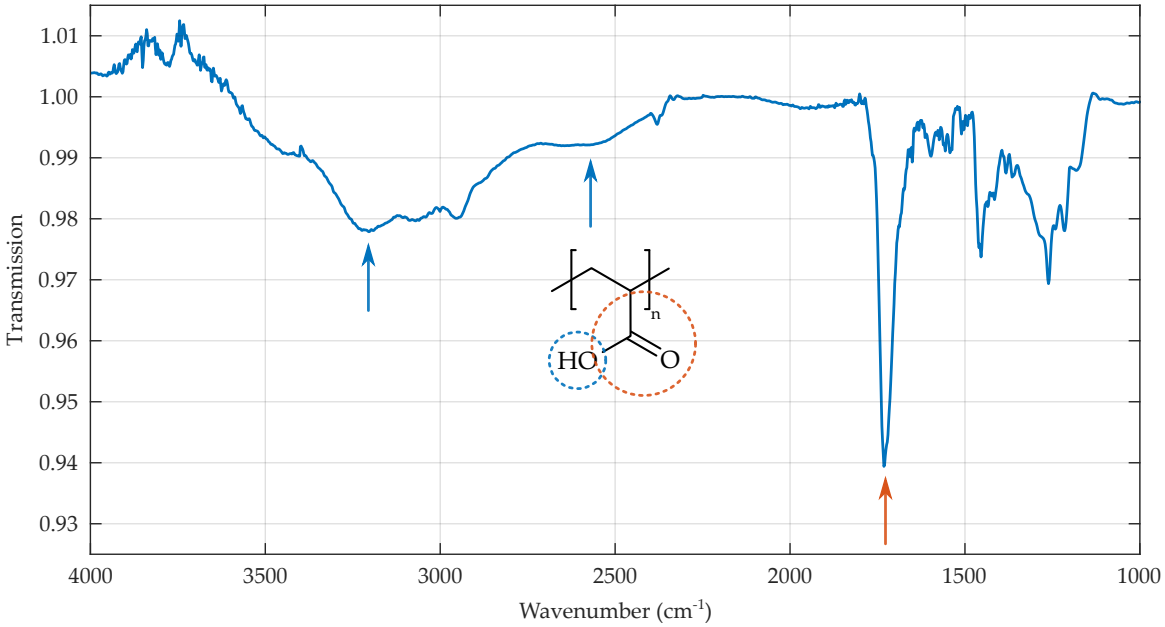

Figure A.1: FTIR spectra of PAA. Measurement taken by Katarina Logg at Chalmers Materials Analysis Lab. Data analysis was done by me.

A.2 FTIR of PHEAA

Poly(*N*-hydroxyethylacrylamide) has three notable IR regions (Figure A.2), a wide band from 3700 cm^{-1} to 3100 cm^{-1}, a peak at 1650 cm^{-1} and a peak at 1540 cm^{-1}.

A wide band from 3700 cm^{-1} to 3100 cm^{-1} is associated with N-H and O-H vibrations (blue). The peak at 1650 cm^{-1} is associated with C=O stretching in the carbonyl group (red) of an amide. The peak at 1540 cm^{-1} is associated with CNH deformation of an amide (yellow)[153].

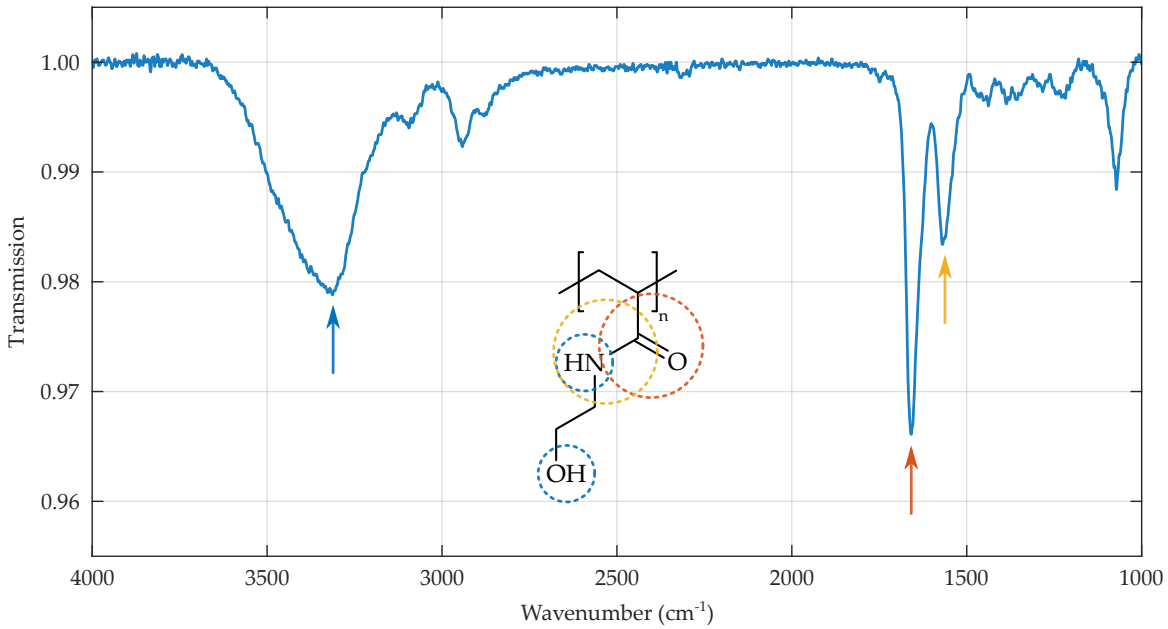

Figure A.2: FTIR spectra of PHEAA. Measurement and data analysis were done by me.

A.3 FTIR of PNIPAM

Poly(*N*-isopropylacrylamide) has three notable IR regions (Figure A.3), a weak band from 3700 cm^{-1} to 3100 cm^{-1}, several smaller peaks from 3000 cm^{-1} to 2800 cm^{-1}, a peak at 1660 cm^{-1} and a peak at 1545 cm^{-1}.

A wide band from 3700 cm^{-1} to 3100 cm^{-1} is associated with N-H vibrations (blue). A weak band from 3000 cm^{-1} to 2800 cm^{-1} is associated with C-H stretching (this band is quite common in polymers, but it is characteristic of PNIPAM due to the two methyls). The peak at 1660 cm^{-1} is associated with C=O stretching in the carbonyl group (red) of an amide. The peak at 1545 cm^{-1} is associated with CNH deformation of an amide (yellow)[153].

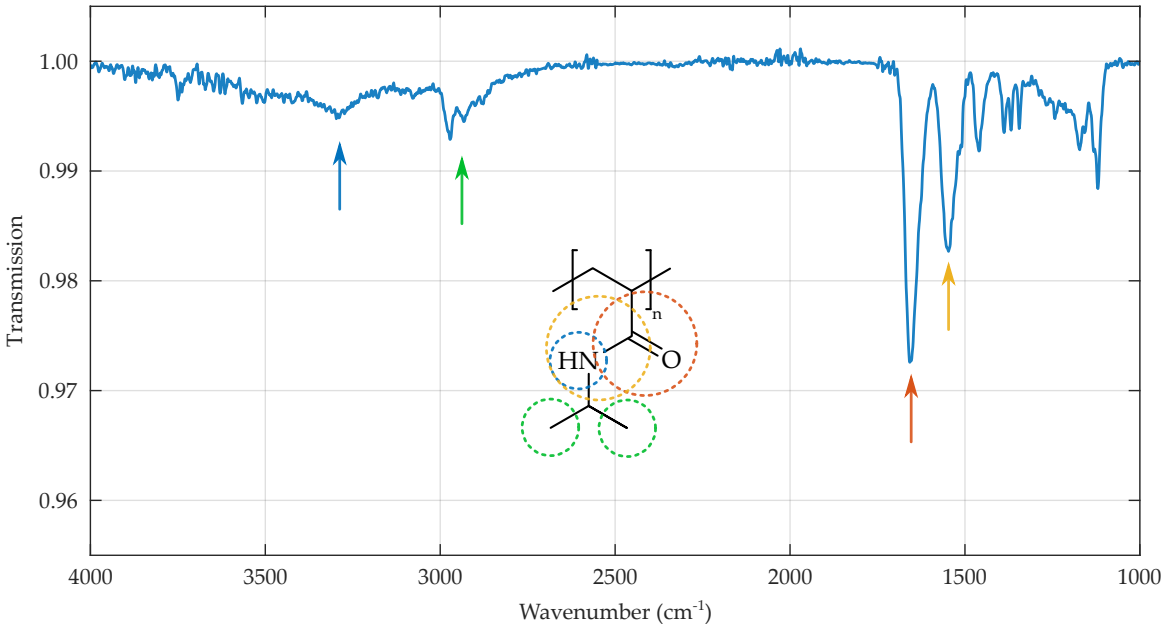

Figure A.3: FTIR spectra of PNIPAM. Measurement and data analysis were done by me.